





Article

A Multi-Proxy Approach to Reconstruct Hypoxia on the NW Black Sea Shelf over the Holocene

Sarah Robinet ^{1,2,*} , Alice Ofélia Matossian ^{1,3,*}, Arthur Capet ⁴, Lei Chou ⁵ , François Fontaine ¹, Marilaure Grégoire ⁴, Gilles Lepoint ⁶ , Natalia Piotrowska ⁷, Audrey Plante ^{1,5}, Olaya Román Romín ¹ and Nathalie Fagel ¹ 

- ¹ AGEs, Clay, Geochemistry and Sedimentary Environment, Department of Geology, University of Liège, Allée du Six Août 14, B-4000 Liege, Belgium; francois.fontaine8@gmail.com (F.F.); audrey.plante974@gmail.com (A.P.); olaya.roman@gmail.com (O.R.R.); nathalie.fagel@uliege.be (N.F.)
 - ² Unit of Physical and Quaternary Geography, Department of Geography, University of Liège, Clos Mercator 3, B-4000 Liege, Belgium
 - ³ Renard Centre of Marine Geology, Department of Geology and Soil Science, Ghent University, Krijgslaan 281, B-9000 Gent, Belgium
 - ⁴ Modelling for Aquatic Systems (MAST), Department of Astrophysics, Geophysics and Oceanography, University of Liège, Allée du Six Août 19, B-4000 Liege, Belgium; acapet@uliege.be (A.C.); mgregoire@uliege.be (M.G.)
 - ⁵ Service of Biochemistry and Modelling of the Earth System, Department of Geosciences, Environment and Society, Université Libre de Bruxelles, Avenue F.D. Roosevelt 50, CP 160/02, B-1050 Brussels, Belgium; lei.chou@ulb.be
 - ⁶ Laboratory of Oceanology, Department of Biology, Ecology and Evolution, University of Liège, Allée du Six Août 11, B-4000 Liege, Belgium; g.lepoint@uliege.be
 - ⁷ GADAM Centre of Excellence, Department of Radioisotopes, Institute of Physics, Silesian University of Technology, Konarskiego 22B, 44-100 Gliwice, Poland; natalia.piotrowska@polsl.pl
- * Correspondence: sarah.robinet@uliege.be (S.R.); alice.matossian@ugent.be (A.O.M.)



Citation: Robinet, S.; Matossian, A.O.; Capet, A.; Chou, L.; Fontaine, F.; Grégoire, M.; Lepoint, G.; Piotrowska, N.; Plante, A.; Román Romín, O.; et al. A Multi-Proxy Approach to Reconstruct Hypoxia on the NW Black Sea Shelf over the Holocene. *J. Mar. Sci. Eng.* **2022**, *10*, 319. <https://doi.org/10.3390/jmse10030319>

Academic Editor:
Juan Santos-Echeandia

Received: 14 January 2022
Accepted: 18 February 2022
Published: 23 February 2022

Publisher's Note: MDPI stays neutral with regard to jurisdictional claims in published maps and institutional affiliations.



Copyright: © 2022 by the authors. Licensee MDPI, Basel, Switzerland. This article is an open access article distributed under the terms and conditions of the Creative Commons Attribution (CC BY) license (<https://creativecommons.org/licenses/by/4.0/>).

Abstract: Coastal hypoxia is a worldwide concern. Even though seasonal hypoxia has been reported on the northwestern Black Sea shelf since the 1970s, little is known about oxygenation in this area over the Holocene. With a multiproxy approach, this work aimed to detect potential hypoxic events in two gravity cores. Our results demonstrate that the most common proxies of hypoxia are irrelevant for the Black Sea coastal environment. For instance, the *Ammonia-Elphidium* index appears to be inappropriate. We assume a salinity bias due to the influence of freshwater inputs. Likely, the redox sensitivity of vanadium is obscured by the dominant supply of detrital elements. However, the size distribution of framboidal pyrites gives clear indications of the oxygenation of the water column. Indeed, the absence of framboidal pyrites in the core located at the Danube mouth suggests permanent oxic conditions over the last 2 ka. On the contrary, in the core located in the Odessa Bay, the two observed ranges of pyrite sizes evidence an alternation between anoxic (mean diameter $3\text{--}6 \pm 1\text{--}2 \mu\text{m}$) and hypoxic or oxic (mean diameter $6\text{--}10 \pm 3\text{--}5 \mu\text{m}$) conditions in bottom waters over the last 7 ka. Therefore, this proxy reveals different oxygenation levels for these proximal sites.

Keywords: Black Sea shelf; anoxia; hypoxia; sedimentary core; foraminifera; framboidal pyrite; iron speciation; trace metal

1. Introduction

In the global ocean, dissolved oxygen plays an essential role in aerobic respiration and thus in ecosystem equilibrium, biodiversity preservation and organic matter degradation. Moreover, oxygen interacts with biogeochemical cycles. Currently, ocean deoxygenation is a growing concern: decreasing oxygen concentration in different types of marine environments affects fisheries and consequently the economy and food safety. The increase in oxygen loss is attributed to climatic warming and excessive nutrient discharges to the coastal area [1]. The decline in oxygen concentration concerns mainly the oxygen minimum

zones (OMZs), fjords, coastal areas and restricted marine basins such as the Baltic Sea or the Black Sea. In situ measurements of oxygen concentration show an increase in the size of areas affected by oxygen depletion and in the duration of these low-oxygen conditions [1].

There are different terms used to define the levels of deoxygenation. Anoxia refers to the total absence of oxygen, while the term hypoxia is used when the oxygen level is sufficiently low to badly affect most organisms. As the tolerance of each species is different, a threshold of 2 mg L^{-1} of oxygen ($63 \mu\text{mol L}^{-1}$) has been chosen [1,2]. Hypoxia can occur at variable frequencies and durations [3], but is seasonal in half of the documented cases [2].

Studies of the Black Sea deep basin have often focused on the establishment and intensity of anoxia [4–6] as well as on the oscillations of the chemocline separating oxygenated surface waters from anoxic and hydrogen sulphide-rich waters [7]. They have shown that the edge of the shelf can be submerged by anoxic water from the deep basin [8,9]. Although the long-term evolution of shelf oxygenation is not known, seasonal hypoxia has been recorded on the northwestern Black Sea shelf since the 1970s [10]. This shelf (<100 m deep) extends over 127,000 km² and receives large inputs of freshwater and nutrients via the Danube, the Dniestr, the Bug and the Dniepr [11], stimulating local primary production. During winter and spring, shelf bottom waters are well oxygenated due to the vertical mixing by storms and strong winds. In early summer, a thermal stratification (i.e., thermocline) sets in, and bottom waters are separated from surface waters. Below the thermocline, the oxic degradation of organic matter consumes oxygen along the stratified season, eventually reaching hypoxic or anoxic conditions by the end of summer or early autumn [12,13]. Although the current seasonal hypoxia is well studied, little is known about the occurrence of hypoxic events on the Black Sea shelf during the Holocene.

This work aims to reconstruct the history of oxygenation on the shelf using sedimentary cores. As the recent seasonal hypoxia was reported to develop, particularly near the coast [12], two coastal sites were chosen for this study. The oxygenation level of past bottom waters can be estimated with proxies, i.e., indicators influenced by the oxygen level and preserved in the sediment. Several biological, sedimentological and geochemical proxies have been proposed in the literature (see [14] for a review): the preserved remains of benthic and planktonic organisms (e.g., foraminifera), the sedimentary features (e.g., laminations), the chemistry and mineralogy of the sediment (e.g., sulphides and redox-sensitive trace elements), the pigments and lipid biomarkers, the organic C, N and their isotopic values. In this work, we tested some of the proxies (Figure 1) to detect past periods of oxygen depletion potentially recorded in the sediments of the NW Black Sea shelf. In the following section, the proxies selected in this study are first briefly reviewed. Then, the two studied sedimentary cores are described, and their age-depth models are presented. Results obtained from the different proxies are exposed. We finally discussed the usefulness of the different proxies in the context of the Black Sea shelf.

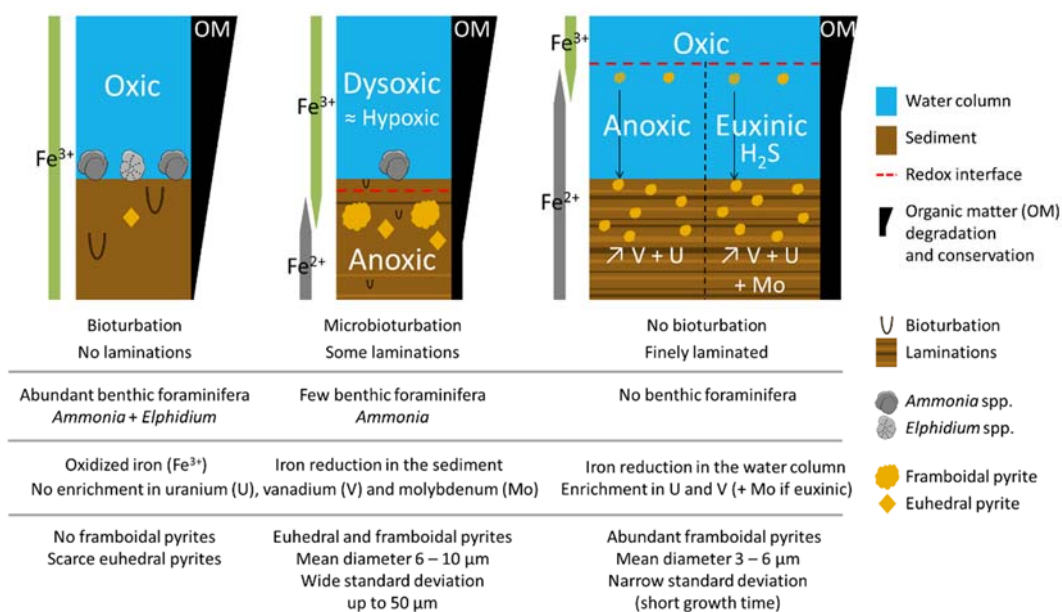


Figure 1. Schematic description (not at scale) of proxies used in the literature and investigated in this work to determine the oxygenation level of bottom waters: presence or absence of bioturbation, laminations [15] and benthic foraminifera [16]; organic matter content [17]; enrichments of trace metals such as vanadium (V), uranium (U) and molybdenum (Mo) [18]; iron redox state; abundance and size of framboidal pyrites depending on the position of the redox interface, i.e., the transition between well-oxygenated water and hydrogen-sulphide rich water [19,20]. The relevance of the proxies used for our case study is discussed in the Discussion section.

2. Potential Proxies for Bottom Water Oxygen Level

The following biological, geochemical and mineralogical proxies have been used in the literature to infer the oxygen level of bottom waters and were tested in this work. Among the proposed proxies, none is able to detect seasonal hypoxia given that a sediment sample corresponds to an average of several years and geochemical exchanges between the sediment and the overlying water occur continuously through sedimentation, bioturbation and benthic fluxes. Moreover, the sediment is affected by diagenesis and compaction after its deposition. Other parameters, for example, the sediment input, rate and resuspension, salinity variations and water stratification, might influence the proxies. In this study, the oxygenation level inferred from proxies was divided into four categories (Figure 1): oxic (well-oxygenated), dysoxic (moderate oxygen depletion, considered here as a synonym of hypoxic), anoxic (no oxygen) and euxinic (no oxygen with the presence of hydrogen sulphide).

2.1. Biological Proxy: Benthic Foraminifera

Organisms have different sensitivities with respect to oxygen depletion, and their identification in the sediment can indicate the evolution of the oxygen level over time. For example, Rabalais et al. [21] and Sen Gupta et al. [16] observed a relationship between oxygen content and foraminifera assemblage on the Gulf of Mexico shelf. Consequently, Sen Gupta et al. [16] developed the *Ammonia-Elphidium* index (here referred to as the A-E index). *Ammonia* species are known to be more resistant to oxygen restriction than most of the other foraminifera species and, in particular, those of the genus *Elphidium* (Figure 1). Thus, the A-E index allows one to identify the hypoxic events in shallow marine environments. The two genera are observed in large numbers in the Black Sea [22].

We use the A-E index proposed by Sen Gupta et al. [16]:

$$A - E \text{ index} = \left(\frac{N_A}{N_A + N_E} \right) \times 100, \quad (1)$$

where N_A is the number of individuals from the genus *Ammonia* and N_E is the number of individuals from the genus *Elphidium*.

2.2. Sedimentological Proxies

The preservation of laminations indicates weak or even absent bioturbation by benthic organisms [14,15]. In the case of oxygen depletion in bottom waters, benthic organisms are less abundant or even absent under anoxic conditions. Thus, Zillén et al. [15] used laminated intervals in sediment cores from the Baltic Sea to detect past periods of hypoxia (Figure 1).

2.3. Geochemical Proxies

Organic matter content should be higher in the case of hypoxia (Figure 1) because the lack of oxygen leads to a high preservation of organic matter that is not degraded [17]. For example, in the Baltic Sea, hypoxic periods are characterised by peaks of organic carbon content (C_{org} , 5 to 10% and up to 15% in modern sediments) and oxic intervals by lower C_{org} content (2 to 3%) [23–25].

Redox-sensitive elements are used as geochemical proxies of hypoxia which corresponds to a reducing environment. In this work, trace metal enrichment and iron redox-state were investigated.

First, authigenic enrichment of redox-sensitive trace metals occurs under reducing conditions. In particular, vanadium (V) and uranium (U) are often used as proxies to detect anoxic conditions and molybdenum (Mo) to detect euxinic bottom waters [18].

Second, iron (Fe) is a redox-sensitive element. The oxidised iron (Fe III) is insoluble, while the reduced iron (Fe II) is soluble. Initially, iron is eroded and transported towards adjacent basins with detrital elements, such as aluminium (Al), silicon (Si), potassium (K) and titanium (Ti). If the redox conditions change during deposition or diagenesis, iron can be dissolved and precipitated again. This remobilisation of iron results in an iron signature in the sediment that is different from that of the detrital elements. A first approach is thus to test the correlation between iron and detrital elements with, for example, principal component analysis. Enrichment in iron has been used in several studies (e.g., [24]). For example, Spofforth et al. [26] consider that anoxia is indicated by a high Fe/Al ratio and high sulphur (S) content measured by an X-ray fluorescence (XRF) core scanner.

Moreover, the iron redox state can be determined by iron speciation (e.g., [27]). In the sediment, total Fe can be divided between non-reactive Fe (i.e., iron in silicates such as clay minerals) and reactive Fe (i.e., all iron species that interact in geochemical cycles).

2.4. Mineralogical Proxy: Framboidal Pyrites

Pyrite (FeS_2) forms under reducing conditions. Different pyrite morphologies can be encountered. Framboidal pyrite is the most abundant morphology in sediments and sedimentary rocks and consists of a spherical aggregate of pyrite micro-crystals in a raspberry-like form [28]. The usefulness of framboidal pyrites as a proxy for oxygen-level comes from the fact that the size of framboidal pyrites depends on the oxygen content of bottom waters [19]. The nucleation and the subsequent aggregation of micro-crystals occur just under the redox interface between oxygenated waters and hydrogen sulphide-rich waters, according to Wilkin and Barnes [4]. The size of the framboids depends on the growth time and, thus, the position of the redox interface. In the case of anoxic bottom waters, the redox interface is located in the water column (Figure 1). As framboidal pyrites sink rapidly after their formation due to their density, their growth time is limited, resulting in a smaller size [19]. On the contrary, if the redox interface is located within the sediment, framboidal pyrites have a longer growth time and are thus bigger [19]. Two diagnostic categories of size distributions can be highlighted. Firstly, if the mean diameter is between 3 and 6 μm with a narrow standard deviation, it corresponds to anoxic or euxinic bottom waters. Secondly, if the mean diameter is between 6 and 10 μm , including framboids up to 50 μm in parallel with a wider standard deviation, it indicates dysoxic or oxic bottom

waters [19] (Figure 1). If no framboidal pyrites are found, it is interpreted as an indication of past oxic bottom waters [20] (Figure 1).

3. Materials and Methods

3.1. Study Sites

The two studied cores were retrieved in the framework of the BenthOx Project (FNRS PDR T.1009.15) by a gravity corer on board the RV Mare Nigrum in May 2016, during the EMBLAS-II cruise. Both cores are from the NW Black Sea shelf, less than 5 km from the coast (Figure 2). The MN16-GC7 core (215 cm long) was collected at the mouth of the Danube (at 20.5 m below sea level), and the MN16-GC15 core (297 cm long) was taken in the Odessa Bay (at 19 m below sea level). The gravity corer sampling method does not allow one to preserve the water-sediment interface. However, multicorers (MN16-MC7 and MN16-MC15) better preserve the water-sediment interface [29]. The core names are abbreviated as GC7, MC7, GC15 and MC15 in the following text.

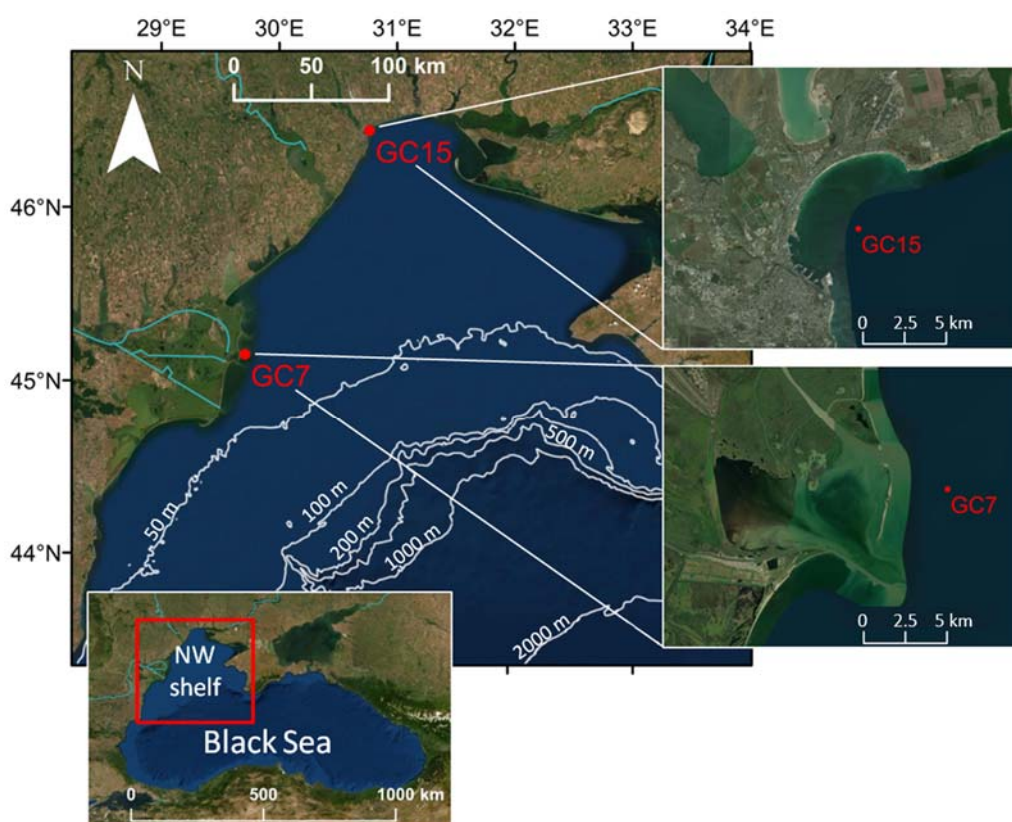


Figure 2. Locations of the gravity cores and multicorers, GC7 and MC7 in front of the Danube mouth (45°12' N, 29°48' E) and GC15 and MC15 in the Odessa Bay (46°31' N, 30°47' E).

3.2. Sampling Strategy and Sedimentological Methods

The cores of 10 cm in diameter were subdivided into two half-cylinders. Plastic sleeves (for X-radiographs and X-ray fluorescence core scanner) and 25 cm long metal boxes (for thin sections) were inserted into one half-cylinder. In the plastic sleeves, the 20 cm at the top of GC7 and 25 cm at the top of GC15 were not scanned. The other half-cylinder was sliced at every centimetre interval. Each slice was divided into four subsamples used for different proxy analyses: (1) the sedimentological analyses (X-ray diffraction and grain size analysis), (2) the geochemical analyses (quantitative measurements and reactive iron extraction), (3) the foraminifera and framboidal pyrite observations and (4) a reserve sample. For the proxy analyses, laminated intervals in GC7 and GC15 were targeted, given that these intervals were assumed to be more likely anoxic/hypoxic, according to Zillén et al. [15]. In addition, reworked shell layers (Units 3 and 5, see Figure 3) in GC15 were not sampled for further

analyses. Finally, additional samples were taken in order to obtain a well-distributed sampling.

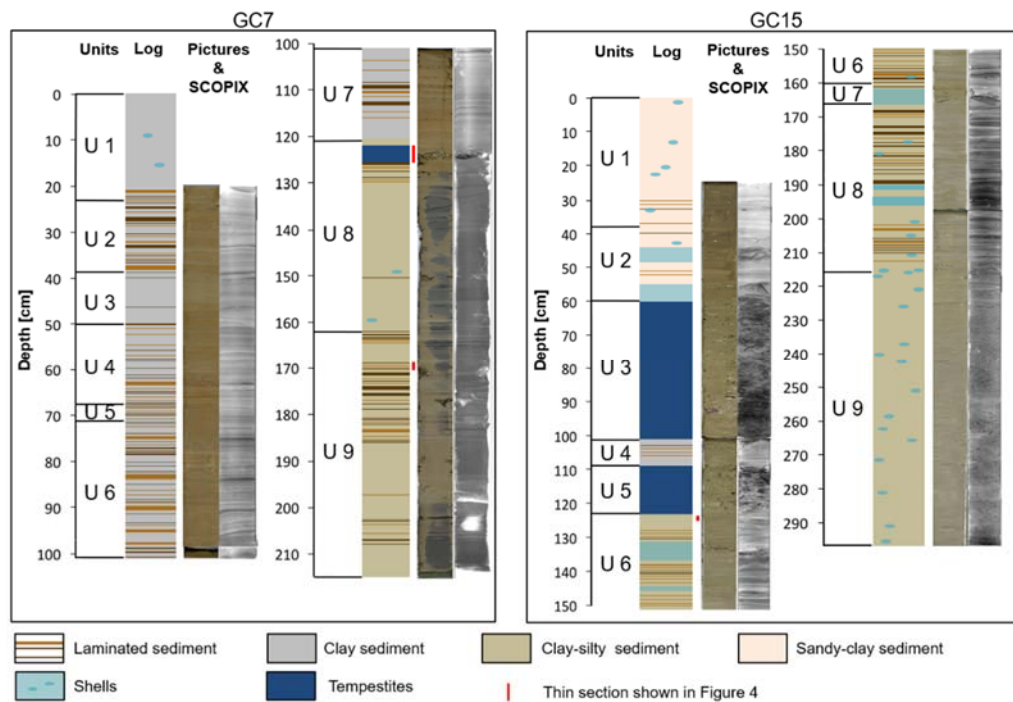


Figure 3. Lithological description with the pictures of the cores and the corresponding SCOPIX images. Nine lithological units were identified in GC7 and in GC15, according to macroscopic observations, SCOPIX and thin sections. For GC7, U1: Homogeneous clay sediment with a few whole shells (SCOPIX unavailable); U2: laminated (mm to pluri-cm) clay sediment; U3: homogeneous clay sediment; U4: laminated (mm to cm) clay sediment; U5: laminated (mm to cm) clay sediment; U6: clay sediment with laminations (mm to cm); U7: clay sediment with laminations (mm to cm) and a pluri-cm level without sedimentary structures; U8: clay-silty sediment with a tempestite (i.e. accumulation of whole shells and shell debris) at the top of the unit (this thin section shown in Figure 4), some laminations (mm to pluri-mm) and a pluri-cm level without sedimentary structure; U9: homogeneous clay-silty sediment with a few laminations (mm to cm). For GC15, U1: Sandy sediment with whole shells and rare laminations (pluri-mm to cm); U2: sandy sediment with a few laminations (pluri-mm), whole shells and shell debris; U3: amalgamated tempestites; U4: laminated (pluri-mm) clay sediment; U5: tempestite; U6: clay-silty sediment with laminations (mm to cm) and some whole shell and shell debris; U7: sediment with whole shells and laminations (mm to pluri-mm); U8: clay-silty sediment with laminations (mm to cm) and some whole shells and shell debris; U9: homogeneous clay-silty sediment with some whole shells and shell debris (not studied in details).

The description of the sedimentary cores is based on macroscopic observations, X-radiographs and thin sections. X-radiographs (SCOPIX) were performed by the EPOC laboratory (University of Bordeaux) on plastic sleeves using an X-ray source (microfocus 130 kV-L9181-02-HAMAMATSU) coupled with a detector (X-ray TDI camera C10650-HAMAMATSU) to obtain high-resolution images (0.92 mm) and the associated grey scale. The thin sections were performed by the EPOC laboratory (University of Bordeaux) and by MKfactory (Stahnsdorf, Germany).

Grain size analyses were performed at every 5 cm interval on 44 samples from GC7 and 27 from GC15 at the University of Liege, using a Malvern Mastersizer 2000 laser grain size analyser coupled to a Hydro S wet dispersion unit. The results were processed using the Mastersizer 2000 software.

3.3. Description of the Cores and Sediment Characteristics

The upper part of the GC7 core (Figure 3) is composed of homogeneous clayey sediment, with laminated (Units 2, 4 to 7) and homogeneous units (Units 1 and 3). At greater depths (Units 8 and 9), coarser levels are interspersed with laminations and a graded shell level interpreted as a tempestite (i.e., storm deposits) at the top of Unit 8. The lamination thickness is millimetric to pluri-centimetric. The identified broken shells belong to bivalves, brachiopods and foraminifera.

In the GC15 core (Figure 3), Units 1 and 2 consist of homogeneous sandy-clay sediment with a few laminations. In Units 3 and 5, the sediment is mainly composed of broken and intact shells. These units are interpreted as multi-decimetric amalgamated tempestites. In the lower part of the core, Units 6 to 8 show laminated clay-silty sediments. The lamination thickness is millimetric to centimetric. A sharp transition is observed between the laminated Unit 8 and the homogeneous Unit 9. The latter has not been studied in detail. No lithological correlation between the two cores was possible since they are located 150 km from each other.

In the thin sections, several sedimentary structures were observed, such as tempestites (Figure 4A), geopetal structures, laminations (Figure 4B) and bioturbations (Figure 4C). Tempestites (top of Unit 8 in GC7 and Units 3 and 5 in GC15) highlight events, including storms, during which energy on the shelf is sufficient to remobilise sediment and shells in a large number. During this kind of energetic event, the water column is mixed. The bottom waters and the remobilised sediment are thus temporarily oxygenated. Moreover, geopetal structures have been observed. They show, in addition to the tempestites, significant remobilisation of the sediment. Numerous bioturbations were observed in thin sections, even in the macroscopically laminated levels. Thus, both cores were impacted by different perturbations and reworked at many depths over several centimetres, especially GC15 with a 40 cm-thick tempestite level (Figure 3, U3).

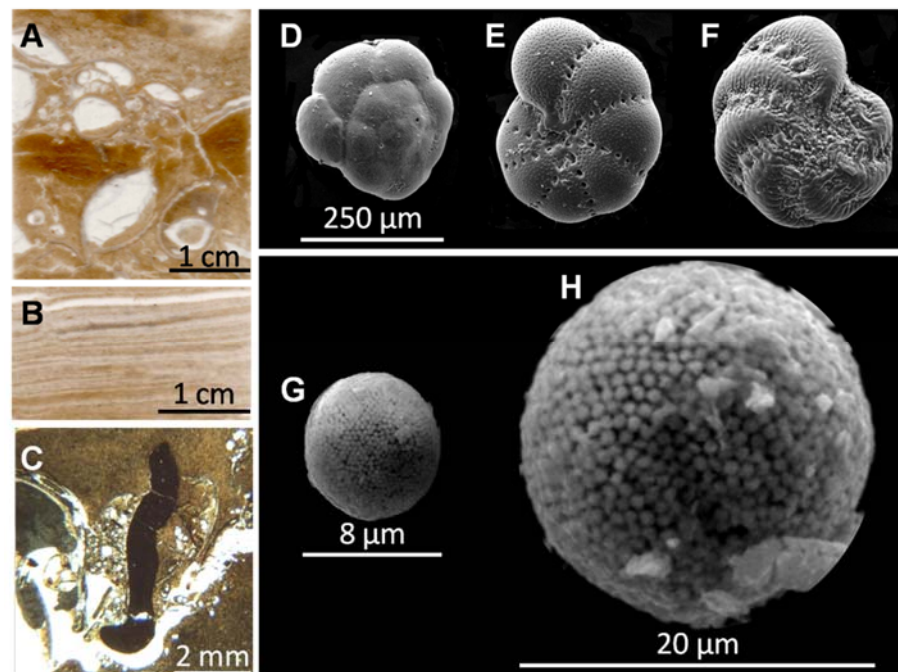


Figure 4. Illustrations of elements encountered in the studied cores. Sedimentary structures observed in thin section by optic microscope (see vertical positions in the cores in Figure 3): (A) tempestite at the top of Unit 8 in GC7; (B) laminations between 169 and 171 cm in GC7 (Unit 9) and (C) bioturbation between 145 and 146 cm in GC15 (Unit 6). Scanning electron microscopy (SEM) images of benthic foraminifera: (D) *Ammonia* spp. and (E,F) two different species of *Elphidium* spp. SEM images of framboidal pyrites: (G) between 1 and 5 cm and (H) between 28 and 30 cm in the GC15 core.

3.4. Core Chronology

For the most recent sediments, ^{210}Pb measurements were conducted on 3 samples from MC7 (at 0.5, 4 and 8 cm depths) and 6 samples from GC15 (at 0.5, 10.5, 20.5, 28, 32 and 34 cm depths). Results of ^{210}Pb dating are presented in Table A1. The radiometric analysis was carried out with a γ spectrometer and a germanium detector at the EPOC laboratory (University of Bordeaux). The ^{210}Pb in excess ($^{210}\text{Pb}_{\text{xs}}$) was calculated as the difference between measured ^{210}Pb and ^{226}Ra . For GC15, a constant sedimentation rate of 0.65 cm/year (from 0 to 25 cm depth (Figure 5) was derived from the $^{210}\text{Pb}_{\text{xs}}$ data, using a CF-CS model (constant flux-constant sedimentation) [30]. For MC7, a sedimentation rate of 0.41 cm/year (Figure 5) was calculated from the regression between 2 measured levels at 0.5 and 8 cm depths.

For the lower part of the core, the AMS ^{14}C dating was performed on shells and on the fine $<63\ \mu\text{m}$ organic fraction of the sediment (OF) at the GADAM Centre (Silesian University of Technology, Poland). For GC7, one shell and six OF samples were dated. For GC15, five shells and seven OF samples were dated (Table A2). At 5 depths, dating was performed both on the shell and OF: at 117.5 cm depth for GC7 and at 57, 166.5, 220.5 and 259.5 cm depths for GC15 (Table A2). For all samples, we used the Marine13 calibration dataset [31] with a global ^{14}C reservoir age of ca. 400 years. Additionally, the local reservoir effect, i.e., the difference between the local shell age and the global Marine13 calibration curve, was added. The local reservoir effect correction (Local ΔR) was estimated by two methods. The first one uses the Marine Reservoir Correction Database (<http://calib.org/marine/>, accessed on 24 October 2019), based on Siani et al. [32] and Jones and Gagnon [33]. The obtained Local ΔR corrections were 126 ± 40 years for GC7 and 57 ± 85 years for GC15. The second one was based on a new method developed by Soulet et al. [34] to estimate the total reservoir ages of the Black Sea bivalve shells. This method uses the $\delta^{13}\text{C}$ determined by isotope ratio mass spectrometer (IRMS). The difference between the shell age and the atmospheric organism's age ($R_{\text{shell-atm}}$, i.e., ΔR) was estimated following the formula of Soulet et al. [34]:

$$R_{\text{shell-atm}} = \Delta R = 400 + \text{Local } \Delta R = 473(\pm 58) - 68(\pm 13) \times \delta^{13}\text{C}_{\text{shell}} \quad (2)$$

The $R_{\text{shell-atm}}$ values have been calculated for four shell samples from the GC15 core (see Local ΔR values in Table A2).

For repeated measurements on different samples from the same depth, the weighted average age (WiTi ^{14}C Age) was calculated and used in the age model (Table 1).

Table 1. Examples of ^{14}C dating performed on GC7 and GC15 by the GADAM Centre (Poland). The dating was done on the OF (fine $< 63\ \mu\text{m}$ organic fraction of the sediment) and on bivalve shells. The WiTi ^{14}C age corresponds to the weighted average of ^{14}C age of two samples from the same depth. A complete dataset with all the dated samples is summarised in Table A2.

Core	Laboratory ID	Depth (cm)	Material Dated	^{14}C Age (BP)	Error	WiTi ^{14}C Age (BP)
GC7	GdA-5385	41	OF	2930	45	2730 \pm 35
	GdA-5812		OF	2640	30	
GC15	GdA-5040	57	shells	2110	30	2260 \pm 30
	GdA-5816A		shells	2410	30	

A deviation between the shell age (T_{shell}) and the OF age (T_{OF}) was systematically observed in GC7 and GC15. The $Deviation_{\text{OF-shell}}$ was calculated according to the following formula:

$$Deviation_{\text{OF-shell}} = (T_{\text{OF}} - T_{\text{shell}}) \pm \sqrt{\text{error}_{\text{OF}}^2 + \text{error}_{\text{shell}}^2} \quad (3)$$

Except for the sample positioned at 57 cm in the GC15 core, the OF was always older than the shells. For example, at 117.5 cm depth in GC7 (Table A2), the T_{shell} and the T_{OF}

are, respectively, equal to 665 ± 30 ^{14}C BP and 3615 ± 50 ^{14}C BP. Thus, the calculated $Deviation_{OF-shell}$ corresponds to 2950 ± 60 ^{14}C BP.

In the age-depth model of GC15, the OF age at 191.5 cm was rejected to avoid an age reversion. For this core, several values of the $Deviation_{OF-Shell}$ were obtained: -690 ± 50 ^{14}C BP (57 cm depth), 765 ± 57 ^{14}C BP (166.5 cm depth), 1270 ± 72 ^{14}C BP (220.5 cm depth) and 1015 ± 64 ^{14}C BP (259.5 cm depth). In the age-depth model (Figure 5), we did not apply a correction for the deviation between the shells and the OF, and we only took into account the dating on the shells as their ages are here considered more reliable than the OF ages. For the GC15 core, at the 57 cm depth, the fact that the OF was younger than the shell might be due to the reworking of the sediment as observed with the SCOPIX (Figure 3). Thus, the shell age at 57 cm was rejected.

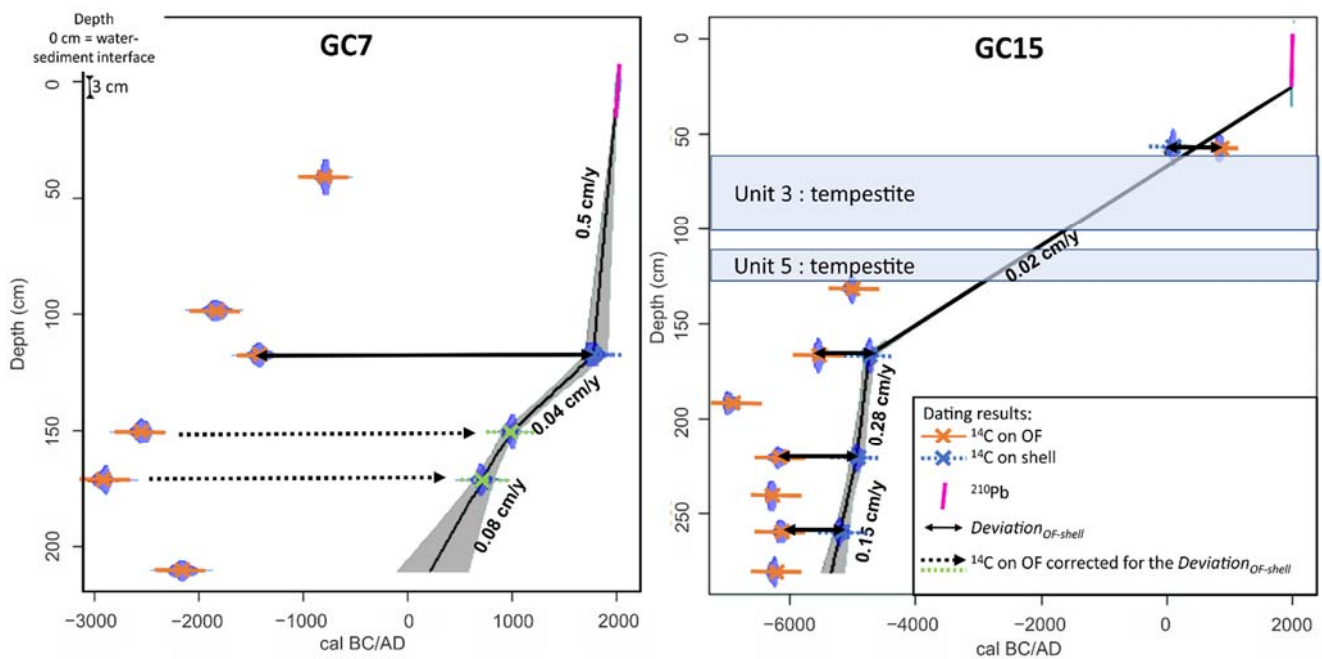


Figure 5. Age-depth models of GC7 (left) and GC15 (right) cores calculated with the Software CLAM version 2.2 [35]. The black line corresponds to the age-depth model (linear regression). The 95% confidence interval (2σ) is defined by the grey area around the age-depth model. The ages taken into account in the model are the ^{210}Pb ages (fuchsia) and ^{14}C calibrated ages on shells (blue). For the GC7 age-depth model, two ages were corrected for the $Deviation_{OF-shell}$ (2950 ± 60 years): 150.5 and 171.5 cm depths (green). The dating result at 117.5 cm depth in GC7 is the only one made on a shell. The orange ages correspond to the results removed from the final age-depth model (OF). The age reservoir effect (global and local) has been corrected for all measurements.

To construct the age-depth model of GC7, the OF ages at 98.5 and 210 cm were rejected to avoid an age reversion (i.e., incoherent younger age at greater depth). Because of the rarity of shells in GC7, we had only one reliable dating in this core at 117.5 cm. We applied the $Deviation_{OF-Shell}$ calculated at 117.5 cm to the OF ages at 150.5 and 171.5 cm in order to have more points to build the age-depth model (Figure 5).

The $Deviation_{OF-shell}$ varies depending on the location (it is ~ 3000 years for GC7 and ~ 1000 years for GC15) but also on the depth (Table A2). Therefore, applying the same correction for the $Deviation_{OF-Shell}$ on several OF ages from different depths, as done with GC7, could potentially misrepresent the age-depth model. To build a coherent age-depth model, we need to consider the age of the shells, which are more reliable as they are younger. However, for the GC7 core, only one shell has been found and dated, and no age-depth model could be produced unless the OF ages were corrected using the $Deviation_{OF-Shell}$.

The age-depth models were calculated with the software CLAM version 2.2 [35]. The year of core collection (2016 AD with an uncertainty of 5 years) corresponds to the water-

sediment interface, i.e., the depth 0 cm of the MC. The models were extrapolated to the deepest dated level (Figure 5). As reworked material has been dated, the age-depth models have certain limitations: they only indicate when the dated material was formed and not when it was deposited. Thus, these age-depth models (Figure 5) have to be used carefully.

3.5. Methods to Investigate Anoxia/Hypoxia Conditions

The following methods were used in this study to detect the proxies presented in Section 2.

3.5.1. Biological Proxy: Benthic Foraminifera

Analyses were performed on >10 g of humid sediment sieved at 250, 150 and 63 μm on 12 samples for GC7 and 8 for GC15. The sediment was observed with a binocular ($\times 45$) and with a scanning electron microscope (SEM). A morphological analysis of the shells on the fraction > 150 μm allowed one to identify the foraminifera at a gender level. Two hundred individuals per sample were counted, when it was possible, in order to correctly apply the A-E index [16].

3.5.2. Geochemical Proxies

The organic carbon content and the C/N atomic ratio were measured on decarbonised samples using an elemental analyser (Vario Microcube C-N-S, Elementar Analysensysteme, GMBH, Hanau, Germany) at the Laboratory for Oceanology, University of Liège, Belgium. The upper 97 cm of GC7 were sampled at every cm interval and the upper 60 cm of GC15 at every 2 cm. Some samples were also analysed in the lower part of both cores (Table A3).

X-ray fluorescence (XRF) core scanner measurements were performed by the EPOC Laboratory (University of Bordeaux, France). The sediment in the plastic sleeves was covered by a 4 μm ultralene film before being scanned at high resolution by an AVAATECH XRF core scanner (third generation, rhodium X-ray tube, silicon detector X PIPS–Canberra). Relatively light elements (e.g., Al, Ti and Fe) were detected with a scan at 10 kV (2000 μA and 20 s for GC7, 1000 μA and 10 s for GC15). The applied correction was the division, at each depth, of the number of counts of a specific element by the sum of counts for all elements analysed at that depth, then multiplied by the average sum:

$$\text{corrected counts} = \frac{\text{counts}}{\sum \text{counts for all elements}} \times \overline{\sum \text{counts for all elements}} \quad (4)$$

The advantages of the XRF core scanner are the continuity and the high resolution of data (1 mm for GC7 and 5 mm for GC15). We tested two hypotheses on our XRF data:

1. It should be possible to distinguish Fe with a detrital signature from Fe remobilised due to changes in redox conditions;
2. High Fe/Al ratio in our cores could be used as a proxy for anoxia as in Spofforth et al. [26].

To challenge the first hypothesis, principal component analyses (PCA) were performed on XRF core scanner data using the R software (PCA function in the FactoMineR library). We considered that Fe has a detrital signature if it is correlated with Al, Si, K and Ti while, if there is no correlation, we assumed that Fe was remobilised after its initial deposition due to changes in redox conditions.

For the second hypothesis, we investigated the meaning of Fe/Al variations in the high-resolution XRF core scanner data. Al is a light element with a high coefficient of variation in the data compared to Fe. Therefore, the Fe/Al ratio was dominated by the noisy variations of Al in both cores (see Figure A1). PCA analysis and visual inspection showed that changes in Si, K, Ti and Al were close, but Al was the noisiest element. In our case, it was better to use Ti as a denominator to investigate the usefulness of the Fe/Ti ratio as a proxy. A set of samples were taken at the position of Fe/Ti peaks in order to test the consistency with another proxy, i.e., the framboidal pyrite observations.

Bulk elemental analyses were performed on 100 mg of dry sub-sample from 1 cm thick sediment slices at the Geochemical Laboratory of the Central Africa Royal Museum, Brussels, Belgium. Several elements (e.g., Al, S) were measured with a Thermo Iris Advantage Inductively Coupled Plasma–Optical Emission Spectrometry (ICP-OES, 14 samples from GC7 and 8 from GC15). Inductively coupled plasma–mass spectrometry (ICP-MS) analyses were carried out with a Thermo Fisher Scientific X-Series2 ICP-MS (28 samples from GC7 and 17 from GC15) to measure several redox-sensitive elements (e.g., V, Fe, U). The low range of elemental variations measured by ICP-OES and ICP-MS did not allow the calibration of XRF core scanner data.

Laser ablation (LA-ICP-MS) was used on 3 resin-embedded blocks (high-resolution data over 1 cm) to determine the Mo concentration. Mo was measured on three samples representative of: (1) the whole GC7 (no framboidal pyrites), (2) levels in GC15 showing large framboidal pyrites and (3) levels in GC15 containing small framboidal pyrites (see hereafter for interpretation of framboidal pyrite proxy).

For V, U and Mo, enrichment factors (EF) were calculated with respect to the average upper crust composition [36]:

$$EF = \frac{\left(\frac{X}{Al}\right)_{\text{sample}}}{\left(\frac{X}{Al}\right)_{\text{upper crust}}} \quad (5)$$

Iron sequential extraction was carried out to determine the reactive iron speciation using the method of Kraal et al. [27] modified from Claff et al. [37] in 11 samples from GC7 and 15 samples from GC15. Four iron fractions were separated: Fe_H (easily extractable fraction with labile ferrous, i.e., FeS and siderite, and ferric iron, i.e., ferrihydrite, akaganeite and lepidocrocite), Fe_{org} (iron bound to organic matter), Fe_{ox} (hematite and goethite) and Fe_{pyr} (pyrite). The different fractions were analysed by atomic absorption (Analytik Jena AA400 model, University of Liège). Reactive iron (Fe_{reactive}) was calculated as:

$$Fe_{\text{reactive}} = Fe_{\text{H}} + Fe_{\text{org}} + Fe_{\text{ox}} + Fe_{\text{pyr}} \quad (6)$$

3.5.3. Mineralogical Proxy: Framboidal Pyrites

Pyrite was first detected using X-ray diffraction (XRD). XRD analyses were carried out every 5 cm on powdered samples (44 for GC7 and 27 for GC15) using a Bruker D8 Advance Eco (Cu X-ray tube, $K\alpha = 1.54 \text{ \AA}$, scan between 2° and $70^\circ 2\theta$, LinxEye XE detector) at the University of Liege (Mineralogy and Crystallography Laboratory and Clay, Geochemical and Sedimentary Environments Laboratory). Diffractograms were analysed with the EVA v.3.2. software (Bruker AXS GmbH) and the Crystallography open database.

Framboidal pyrites of 8 samples from GC7 and 15 samples from GC15 were observed with an SEM (ESEM-FEG XL30 model, at 15 kV, with a working distance of 10 mm) at the University of Liège. Moreover, samples from the top 4 cm (samples from 0–2 and 2–4 cm depths) of the multicorers MC7 and MC15 were observed to investigate the most recent sediments. Samples were sieved at $63 \mu\text{m}$. The clay fraction ($<2 \mu\text{m}$) was removed by successive centrifugations ($8 \times 8 \text{ min}$ at 700 rounds per minute). The fraction between 2 and $63 \mu\text{m}$ was conserved and coated with carbon to allow the detection of framboidal pyrites with the back-scattered electron (BSE) mode. In the BSE mode, pyrite seemed brighter than the surrounding minerals due to its relatively higher atomic number [38]. Energy-dispersive X-ray spectrometry (EDS) analysis confirmed the identification of framboidal pyrites when needed. Generally, a minimum of 100 diameters are measured per sample in studies using this proxy [19,20]. In this work, 30 diameters per sample, i.e., the minimum statistically recommended [39], were measured at $3000\times$ magnification. The mean between two measured diameters per pyrite was calculated.

4. Results

4.1. Benthic Foraminifera

The number of individuals observed varied between the two cores depending on the depth. Few individuals were found in the different granulometric fractions ($>63 \mu\text{m}$, $>150 \mu\text{m}$, $>250 \mu\text{m}$) of GC7 (Figure 6B). On the contrary, for the GC15 core, several hundreds to thousands of individuals were observed (Figure 7B). The most abundant genus found in GC7 and GC15 is the genus *Ammonia* (Figure 4D). It accounts for more than 93% of the counted foraminifera. The genus *Elphidium* (Figure 4 E,F) constitutes 0.5 and 1.8% of the individuals, respectively, for GC7 and GC15 (0–1 individual in GC7 and 0–11 in GC15; Figures 6B and 7B; Table A4). The remaining percentage of individuals corresponds to genus *Nonion* or to other minor unidentified genera (Table A4). The computed A-E index varies between 92 and 100% for GC7 and between 94 and 100% for GC15 (Table A4).

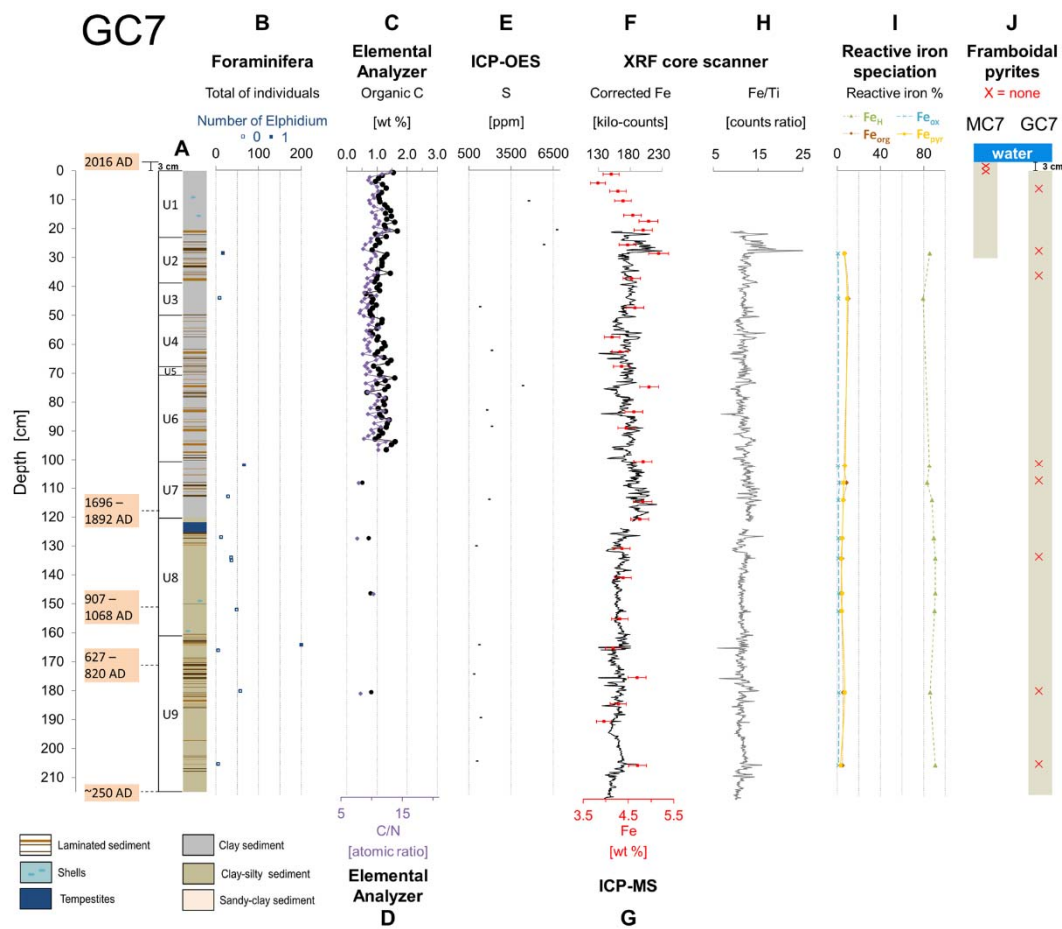


Figure 6. Results of selected proxies for the GC7 core: (A) laminations in most of the core (macroscopic observations, SCOPIX and thin sections); (B) relatively low number of benthic foraminifera, including no or only one *Elphidium* individual; (C) slight decrease with depth of organic carbon content (mean = 1.1 wt % C) and (D) C/N atomic ratio (Elemental Analyser); (E) relatively low total S concentration (ppm, error bar smaller than symbol) measured with ICP-OES compared to GC15; (F) corrected kilocounts of Fe (XRF core scanner) showing no correlation with (G) the total Fe concentration measured by ICP-MS (wt %, with the error bar); (H) Fe/Ti (XRF core scanner) variations; (I) homogeneous reactive iron speciation with ~80% of Fe_H (FeS , siderite, ferrihydrite, akaganeite and lepidocrocite) and low abundance of Fe_{org} (iron bound to organic matter), Fe_{ox} (hematite and goethite) and Fe_{pyr} (pyrite); (J) no framboidal pyrites observed (SEM) nor in the 0–2 and 2–4 cm of MC7, neither in several samples from GC7 (0 cm on the scale on the left, i.e., top of GC7, does not correspond to the water-sediment interface).

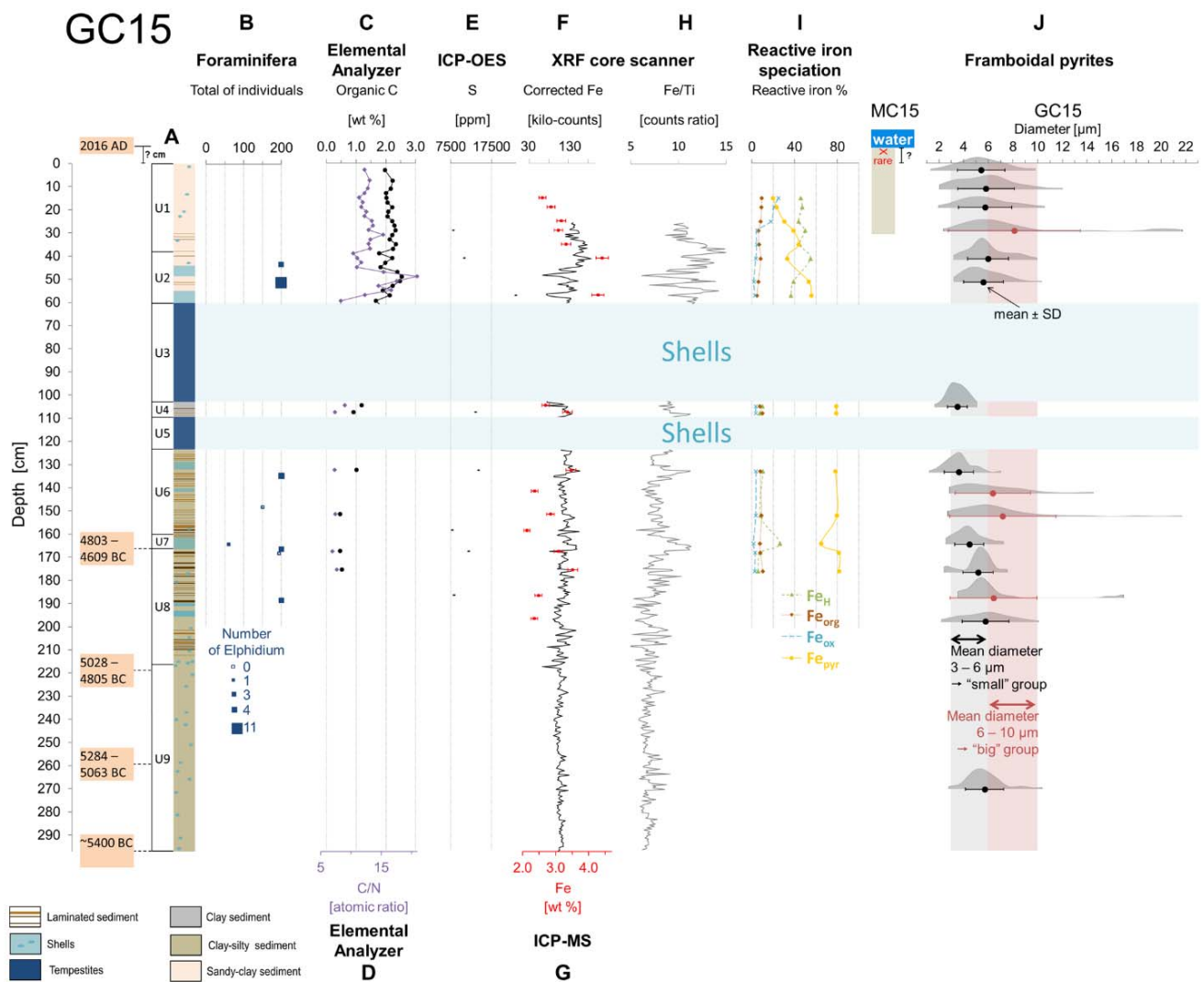


Figure 7. Results of potentially useful proxies for the GC15 core: (A) laminations in some parts of the core and exclusion of reworked shell layers (macroscopic observations, SCOPIX and thin sections) for other analyses; (B) higher number of benthic foraminifera than in GC7, including 0 to 11 *Elphidium* individuals per samples; (C) decrease with depth of organic carbon content (mean = 1.9 wt % C) and (D) C/N atomic ratio (elemental analyser); (E) relatively high total S concentration (ppm, error bar smaller than symbol) measured with ICP-OES compared to GC7; (F) corrected kilocounts of Fe (XRF core scanner) showing no correlation with (G) the total Fe concentration measured by ICP-MS (wt %, with the error bar); (H) Fe/Ti (XRF core scanner) variations; (I) increase of Fe_{pyr} (pyrite) with depth and decrease of Fe_{ox} (hematite and goethite) and Fe_H (FeS, siderite, ferrihydrite, akaganeite and lepidocrocite), constantly low Fe_{org} (iron bound to organic matter); (J) in MC15, no framboidal pyrite observed by SEM in the 0–2 cm sample just below the water-sediment interface and rare framboidal pyrite in the 2–4 cm sample; in GC15 (0 cm on the scale on the left, i.e., top of GC15, does not correspond to the water-sediment interface), framboidal pyrite size distribution showing two groups: (a) “small” group: mean diameter 3–6 μm and narrow standard deviation (in black), (b) “big” group: mean diameter 6–10 μm with wide standard deviation (in red).

4.2. Geochemical Proxies

C_{org} and C/N atomic ratio data are reported in Table A3. The mean organic carbon content was slightly lower in GC7 (1.1 wt %) than in GC15 (1.9 wt %). The C_{org} content (Figure 6C for GC7 and Figure 7C for GC15) and the C/N ratio (Figure 6D for GC7 and Figure 7D for GC15) decreased with depth in both cores. For GC7, the mean % C_{org} was 1.1 wt % and the mean C/N atomic ratio was 10.1 in the top 97 cm. In the bottom part of the

core, the mean % C_{org} was 0.7 wt % and the mean C/N ratio was 8.5 (note the low number of data). For GC15, in the upper 60 cm, the mean % C_{org} was 2.1 wt % and the mean C/N atomic ratio was 13.3, with a peak of 20.9 indicating a terrestrial organic matter input [40]. Below Unit 3, the % C_{org} (0.8 wt %) and C/N (7.6) were lower.

Three trace metals were targeted: V, U and Mo (Table 2). First, the correlation between these trace elements and Al was tested to check if the trace element behaviour was controlled by the detrital inputs, as shown in Tribouillard et al. [18]. V was highly correlated with Al with R² = 0.94 in GC7 and R² = 0.86 for GC15 (Figure A2), contrary to U and Mo. Thus, V could not be used as an anoxia proxy in our case study. There was a slight enrichment in U in GC15 (EF = 1.5, Table 2). Mo concentration was low in the three representative samples and presented no enrichment (Table 2).

Table 2. Average trace metal concentrations in GC7 and GC15 and corresponding enrichment factors calculated with respect to the average upper crust abundance [36].

Element	Average Upper Crust Abundance [ppm]	GC7		GC15	
		Concentration [ppm]	Enrichment Factor	Concentration [ppm]	Enrichment Factor
V ^a	107	130 ± 8	1.3	80 ± 10	1.1
U ^a	2.8	2.7 ± 0.1	1.0	2.9 ± 0.2	1.5
Mo	1.5	0.86 ^{b,1}	0.6	0.96 ^{b,2} 1.12 ^{b,3}	1.0 1.1
Al ^c	80,400	78,312	/	53,726	/

^a Average of ICP-MS measurements on 28 samples for GC7 and 17 samples for GC15 (samples of 1 cm thick). ^b Average over 1 cm of high-resolution LA-ICP-MS measurements on (1) an “oxic” sample from GC7 (no framboidal pyrites); (2) a “dysoxic” sample from GC15 (big framboids) and (3) an “anoxic” sample from GC15 (small framboids, 163–164 cm depth). ^c Average of ICP-OES measurements on 14 samples for GC7 and 8 samples for GC15 (samples of 1 cm thick).

The correlation between iron and detrital elements was investigated using principal component analysis (PCA) on XRF core scanner data. In GC7 (Figure 8A), and in the bottom part of GC15 (Figure 8C), Fe was not correlated with any detrital elements (i.e., Al, Si, K, Ti); it was rather correlated with S. In the upper part of GC15 (Figure 8B), iron was closer to the detrital element cluster. These results suggest a modification of the iron behaviour with depth in GC15 (Figure 8B,C).

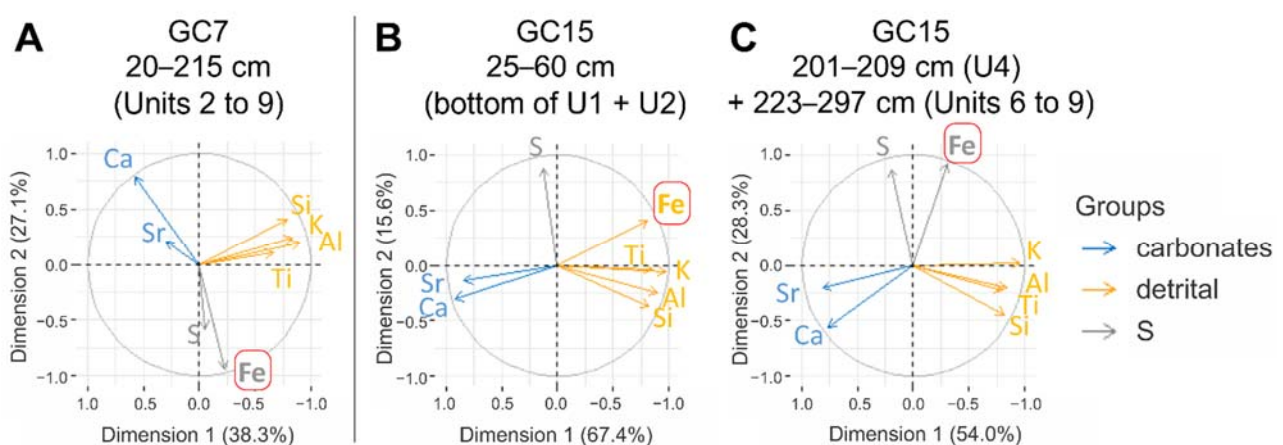


Figure 8. Principal component analyses (PCAs). In both cores, PCAs illustrate the anticorrelation between Fe and calcium (Ca) + strontium (Sr), interpreted as the carbonate cluster (blue). Moreover, Al, Si, K and Ti were strongly correlated with each other and considered as the detrital element cluster (yellow). PCA of (A) the GC7 core showing that Fe was correlated with S and not with detrital elements (65.4% of the variance explained by dimension 1 and 2); (B) the upper part of GC15 where Fe was situated closer to the detrital cluster than to S (83.0% of the variance); (C) the bottom part of GC15 where Fe was closer to S than to detrital elements (82.3% of the variance explained). U = Unit.

The continuous semi-quantitative Fe counts in the XRF core scanner (Figures 6F and 7F) were plotted together with ICP-MS quantitative Fe concentrations (Figures 6G and 8G). It illustrates the absence of possible calibration between the two methods. Moreover, the variations in Fe/Ti measured with the XRF core scanner are displayed in (Figures 6H and 7H).

Reactive iron, i.e., the sum of all the extracted fractions represents, on average, $36 \pm 4\%$ of total iron in GC7 and $38 \pm 6\%$ in GC15. In GC15, reactive iron accounted for 32 to 55% of the total iron (Table A5). In both cores, Fe_{org} was not abundant and remained relatively constant (5 to 10% of reactive iron; Table A5). In GC7, the reactive iron speciation was homogeneous (Figure 6I), dominated by the Fe_H fraction ($87 \pm 4\%$ of reactive iron). The other fractions were less abundant. The pyrite fraction only corresponded to $6 \pm 2\%$ of reactive iron (Table A5). In contrast, GC15 showed an iron reduction with depth (Figure 7I). Indeed, the Fe_{pyr} fraction gradually increased with depth from 20% up to 80% of reactive iron at the expense of the Fe_{ox} and Fe_H fractions (Figure 7I).

4.3. Mineralogical Proxy: Framboidal Pyrites

Pyrite is composed of iron and sulphur. Total Fe content, measured by ICP-MS, varied between 3.8 ± 0.2 and 5.2 ± 0.2 wt % for GC7 (Figure 6G) and between 2.1 ± 0.1 and 4.4 ± 0.2 wt % for GC15 (Figure 7G). Thus, total iron was, on average, more abundant in GC7 (4.5 ± 0.3 wt %) than in GC15 (3.1 ± 0.6 wt %). However, total iron could not be used directly as a proxy because it indicates neither the iron redox-state nor the amount of pyrite. Sulphur, measured by ICP-OES, was, on average, less abundant in GC7 (0.26 ± 0.20 wt %, Figure 6E) than in GC15 (1.21 ± 0.51 wt %, Figure 7E).

In GC7 (Figure 6J), no framboidal pyrites were found in the samples observed with the SEM, which was consistent with the absence of pyrite detected by XRD and the low amount of Fe_{pyr} extracted. The absence of pyrite was also noticed in the uppermost samples collected close to the water-sediment interface in MC7 (Figure 6J).

In GC15, the detection of pyrite by XRD and by sequential extraction ($61 \pm 31\%$ of reactive iron) was confirmed by SEM observations of framboids (Figure 4G,H). The size distributions of the 30 diameters measured per sample (Figure 7J, Table A6) could be divided into two groups. The “small” group included samples with a mean framboid diameter ranging between 3 and 6 μm with a narrow standard deviation (1 or 2 μm), while the “big” group included samples with a mean framboid diameter varying between 6 and 10 μm with a wider standard deviation (3 to 5 μm). In MC15 (Figure 7J), the sample just below the water-sediment interface (0–2 cm) showed no framboidal pyrites. The 2 to 4 cm sample contained rare framboidal pyrites, preventing any calculation of a robust mean.

5. Discussion

5.1. Past Oxygenation of the NW Black Sea Shelf Inferred from the Framboidal Pyrite Proxy

Among all proxies tested in this study, only the presence of framboidal pyrites and their characteristics (i.e., mean diameter and its standard deviation) were directly connected with the level of oxygenation of bottom waters. Up to now, all studies using framboidal pyrites as a proxy were based on the pioneering research of Wilkin et al. [19], who linked the size of framboidal pyrites in modern sediments with the oxygen level of bottom waters in various oxygenated basins. The GC15 results are reported in parallel with the observations of Wilkin et al. [19], where the mean framboid diameters are plotted against the standard deviations of the size distributions (Figure 9). Two categories of oxygenations can be inferred from this graph.

First, the current anoxic-euxinic basins show small framboid diameters and narrow standard deviations [19]. Eleven of the GC15 samples fell in the field of anoxic-euxinic conditions (Figure 9). In a sample considered as representative of the small framboids group in GC15, the absence of Mo enrichment rules out euxinic conditions, according to Tribouvillard et al. [18]. In Figure 9, we define an “anoxic” field around the GC15 results with small mean diameters, including the two samples from GC15 representing the smallest mean diameters.

Second, dysoxic and oxic modern basins produce framboids with larger diameters and wider standard deviations [19]. The fields of dysoxic and oxic conditions are superimposed in Figure 9, even if the oxic field is elongated towards a larger diameter and wider standard deviation. Therefore, it is not possible to distinguish dysoxic environments from oxic ones with only the framboidal pyrite measurements. In Figure 9, we regroup the dysoxic and oxic fields into one field called the “hypoxic-oxic” field, represented by a dashed red ellipse; four samples from GC15 fall into that field.

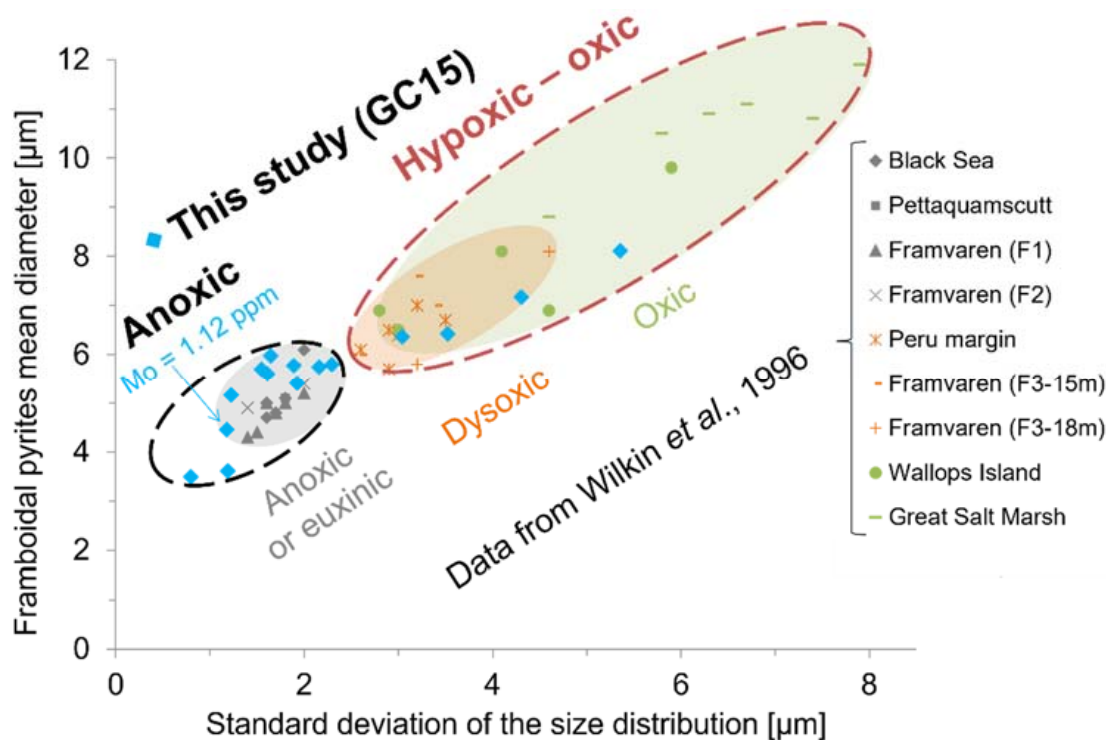


Figure 9. Mean diameter of framboidal pyrites plotted as a function of the standard deviation of the size distribution. Data from Wilkin et al. [19]—a study based on modern sediments—show the characteristics of framboidal pyrites according to the known bottom water oxygenation level. Three oxygenation levels can be defined according to the data of Wilkin et al. [19]: anoxic-euxinic (in grey), dysoxic (in orange) and oxic (in green). The “anoxic” and “hypoxic-oxic” fields are defined based on the results of this study (see text for explanation).

No correlation can be highlighted between the lithological changes in GC15 and the oxygenation variations deduced from framboidal pyrites. Indeed, Figure 7J shows that Units 1, 6 and 8 contain framboidal pyrites belonging to the “small” group (i.e., “anoxic” conditions) as well as to the “big” group (i.e., “hypoxic-oxic” conditions). All the samples from Units 2, 4, 7 and 9 belong to the “small” group (Figure 7J), suggesting anoxic bottom waters, but new samples could reveal framboidal pyrites belonging to the “big” group or no framboids at all. Four of the GC15 samples fall in the “hypoxic-oxic” field, while 11 samples fall in the “anoxic” field (Figure 9). Consequently, the Odessa Bay (GC15 location) underwent an alternation between anoxic and hypoxic to oxic conditions during the past 7.4 ka. The absence or the rarity of framboidal pyrites in the top sediment of MC15 suggests that the current conditions in the Odessa Bay are not favourable for the formation of framboidal pyrites due to a high oxygen level during one part of the year on the shelf or to other controlling factors.

In GC7, the absence of framboidal pyrites can be interpreted as an indication of an oxic water column during sediment deposition, according to the classification of Bond and Wignall [20] (Figure 1). However, Wilkin et al. [19] found framboidal pyrites in modern oxic basins (Figure 9). This contradiction suggests that the oxygenation level is not the

only factor controlling the framboid formation. The absence of pyrite in GC7 might be linked to the lower amount of sulphur in this core compared to GC15 (Figures 6E and 7E). Future studies on the sulphur speciation of the GC7 and GC15 cores should allow the determination of the proportion of sulphur associated with pyrite (e.g., [41]). The observation of the top sediment of MC7 indicates that there is currently no framboidal pyrite formation in front of the Danube mouth.

The sample preparation in this study (i.e., loose sediment, only the fraction between 2 and 63 μm) does not allow us to estimate the abundance/density of framboidal pyrites, which is one of the criteria used in the classification of past oxygen levels defined by Bond and Wignall [20]. Thus, it could be interesting to evaluate the abundance of framboidal pyrites. Moreover, several pyrite morphologies were encountered in the GC15 core: euhedral crystals, loose aggregates of microcrystals, framboidal pyrites (totally, partially or not at all filled-in by pyrite secondary growth) and a cluster of framboidal pyrites (Figure A3). It could also be relevant to systematically report the pyrite morphologies as they may provide some clues about the formation environment.

5.2. Other Proxies Considered as Inappropriate in the Case of the Black Sea Coastal Environment

In our case study of the Black Sea coastal environment, other proxies are not as conclusive as the framboidal pyrite proxy concerning the bottom water oxygenation (Figure 10).

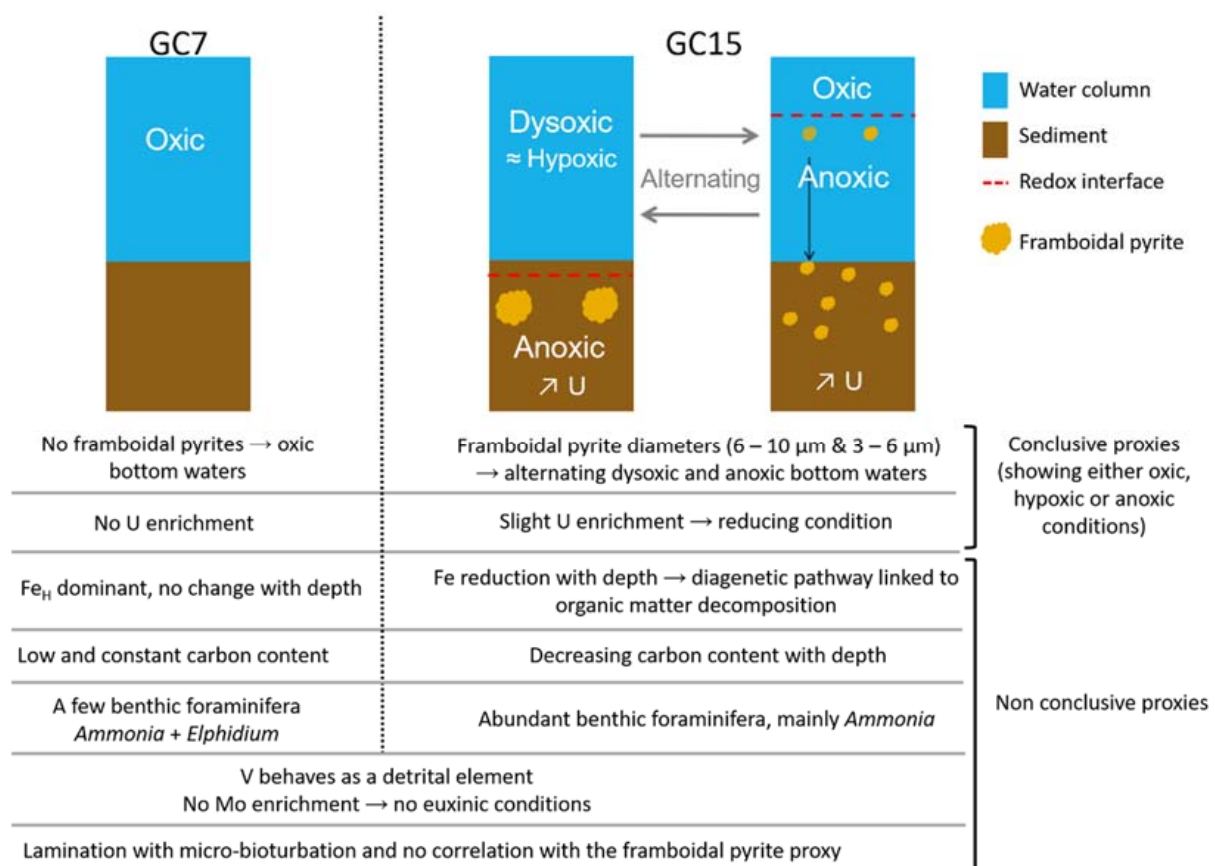


Figure 10. Summary of the different conclusive and non-conclusive proxies tested in GC7 and GC15 and of interpretation of the past oxygenation conditions at the sediment-water interface. The most useful proxies are the framboidal pyrite diameter, U and Mo enrichment. The non-conclusive proxies are the iron speciation, the organic carbon content, the *Ammonia-Elphidium* index, the V enrichment and the presence of laminations. See text for a detailed discussion.

5.2.1. Laminations

The use of the laminated intervals was not relevant in our case to detect hypoxia, but it might be in other cases (as used in the Baltic Sea by Zillén et al. [15]). Indeed, several units of GC7 and GC15 are macroscopically laminated, but bioturbated in thin sections. Moreover, oxic conditions are suggested in both laminated and non-laminated intervals of GC7 (Figure 6A,J). Similarly, there was no relation between the lamination of the sediment in GC15 (Figure 7A) and the occurrence of framboidal pyrites, whatever their size (Figure 7J). Moreover, anoxia was suggested by the small framboidal pyrites observed in U1 and U9 of GC15, and both units were not laminated.

5.2.2. Foraminifera

According to Sen Gupta et al. [16], when the A-E index is close to 100% (i.e., when the genus *Ammonia* is over-represented in the assemblages compared to the genus *Elphidium*), it suggests a hypoxic environment. This was the case in both GC7 and GC15, with an A-E index between 92 and 100%. In GC7, the results were questionable: the number of observed individuals rarely reached 200, and for all analysed samples, either one or no *Elphidium* were identified (Figure 6B; Table A4). Thus, computing this index for GC7 seems to be unreasonable.

As highlighted by Sen Gupta and Platon [42], this index can only be used under strict conditions: high sedimentation rate, water depth less than 30 m, minimally bioturbated sediments and constant salinity. Observations of the thin sections and of the SCOPIX (Figure 3) have shown, respectively, that the sediment is bioturbated and reworked in GC7 and GC15, which may contribute to the erroneous results of the index. Additionally, the average salinity and its variations have a strong impact on the index [42]. This parameter influences the diversity in the assemblage of foraminifera, and a local decrease in salinity on the Black Sea shelf can trigger an impoverishment of the assemblage [22]. At the coring locations, in a proximal environment and next to the mouth of rivers, the average salinity was low, and the fluctuations of salinity were important. The abundance of *Ammonia* spp. and the near absence of *Elphidium* spp. may be due to the higher resistance of the genus *Ammonia* living in mesohaline and polyhaline waters [14], to the decrease of salinity and not necessarily to the lack of oxygen. Moreover, the average salinity (only a few ‰) at the coring location of GC7, i.e., at the mouth of the Danube, may explain the low number of individuals observed in the samples [22]. This relationship between the salinity and the abundance of *Elphidium* was demonstrated by Cronin et al. [43], who used the *Elphidium* genus to reconstruct the variability of the salinity during the last centuries in the Chesapeake Bay (USA). The authors highlighted that the higher the salinity, the higher the abundance of *Elphidium* in the foraminiferal assemblages. Few or no *Elphidium* individuals are found at salinity values $\leq 10\text{‰}$ (closer to the coast).

Parameters other than oxygen concentration and salinity also influence the benthic foraminifera and their assemblages, such as the substrate, temperature, luminosity and nutrient availability [44]. Thus, all these coastal parameters must be considered when interpreting the results of the A-E index. We cannot, therefore, conclude if this index could be used to identify hypoxic events that occurred on the NW Black Sea shelf during the Holocene.

To determine if the A-E index is applicable in the context of the Black Sea shelf, it would be more relevant to take sediment at a greater distance from the mouth of the rivers. This may allow clear documentation of the hypoxic signal in the sediment without the influence of the salinity and its variations. It is also possible that the much lower average salinity of the Black Sea ($\sim 17\text{‰}$), compared to the optimal salinity ($\sim 35\text{‰}$) [44] for most of the foraminifera, renders the use of this index complicated.

5.2.3. Organic Matter

In both cores, C_{org} content decreased with depth. No significant enrichments in organic matter have been measured (max 1.7 wt % for GC7 and max 2.5 wt % for GC15) as compared to the 5 to 10 wt % (up to 15 wt %) recorded in the Baltic Sea during hypoxic periods [23–25]. Thus, we cannot identify short episodes of oxygen restriction on the Black Sea shelf. However, there was slightly more organic carbon in GC15, where the presence of framboidal pyrites suggests oxygen depletion, as compared to GC7, where oxic conditions are assumed.

The C/N atomic ratios indicate, according to the range of values presented in Leng and Lewis [40], the dominance of organic matter with a marine or freshwater origin ($C/N < 12$), except for the peak value observed in GC15, which suggests an input of terrestrial plants ($C/N > 12$).

5.2.4. Trace Metals

Results of trace metals were not conclusive. V behaves mainly as a detrital element and cannot be used as a hypoxia proxy. U was slightly enriched in GC15, suggesting reducing conditions, which is consistent with the framboidal pyrite proxy. U was not enriched in GC7, suggesting conditions different from GC15. Low Mo contents indicate that euxinic conditions are unlikely. Table 3 shows that trace metal concentrations (V, U and Mo) were relatively similar in the intervals considered as representative of: (1) oxic conditions in GC7, (2) hypoxic/oxic conditions in GC15 and (3) anoxic conditions based on the framboidal pyrite proxy. Future research with additional measurements should confirm these findings.

Table 3. Trace metal concentration in three embedded blocks analysed by LA-ICP-MS representative of 3 different oxygenation conditions in bottom waters.

Core	Depth (cm)	Framboidal Pyrites	Oxygenation Level Inferred	Average Concentration (maximum)		
				V	U	Mo
GC7	106.5–107.6	none	oxic	105 (179)	2.0 (30.5)	0.86 (10.67)
GC15	151–151.8	big group	hypoxic/oxic	91 (199)	2.7 (45.8)	0.96 (6.73)
GC15	162–164.2	small group	anoxic	104 (165)	3.0 (57.7)	1.12 (11.28)

5.2.5. Iron Behaviour

In our study, the total iron concentration, as well as Fe/Ti ratio, was not useful for estimating the past oxygenation. The anoxic/hypoxic periods suggested by punctual high Fe/Ti values could not be further validated by the framboidal pyrite observations. Indeed, in GC7, some peaks of Fe/Ti appeared, but no framboidal pyrites were found at the corresponding depths, suggesting oxic conditions. In GC15, at depths where framboidal pyrites were observed, peaks of Fe/Ti and S/Ti were not always present.

Moreover, XRF semi-quantitative data should be used with caution because the counts depend not only on the atomic number of the element but also on many factors, such as water and organic matter contents, grain size and surface irregularities [45]. Furthermore, the low range of elemental variations measured by ICP-MS and ICP-OES did not allow us to calibrate the XRF core scanner data. Consequently, the XRF core scanner data did not seem to be reliable enough to allow the detection of anoxia/hypoxia in this study.

A change in the iron behaviour between the upper and bottom parts of GC15 was suggested by PCA. This is consistent with the occurrence of iron reduction with depth detected by the iron speciation. This iron reduction was linked to the decomposition of organic matter within the sediment during diagenesis [17]. However, it provided no clear indication regarding the water column oxygenation.

Concerning iron speciation, the sequential extraction process of Poulton and Canfield [46] should be used in further research. Following this procedure, the bottom waters of the deposition environment are considered anoxic [47] if the ratio between reactive Fe and total Fe is greater than 0.38. The bottom waters are regarded as euxinic [48] if the ratio between pyrite iron and reactive iron is greater than 0.8. van Helmond et al. [49] successfully used these ratios to conclude that a coastal location in the Baltic Sea underwent anoxia and not euxinia during the Holocene. However, we could not use these ratios in our study because the reactive iron determined following Kraal et al. [27] (see Equation (6)) is not exactly the same as that assessed according to Poulton and Canfield [46].

6. Conclusions

This work, based on the study of two sedimentary cores, highlighted that the Danube mouth (GC7 location) and the Odessa Bay (GC15 location) underwent different oxygenation conditions over the time period covered by the sedimentary record.

Our results demonstrate that the most common biological and geochemical proxies of hypoxia proposed in the literature are irrelevant for the case study of the Black Sea coastal environment. For instance, the *Ammonia-Elphidium* index appears to be unsuitable for the NW Black Sea shelf, mainly in the case of the Danube mouth (GC7), where only a few foraminifera individuals have been found in the sediments. We assume that the foraminiferal assemblages are salinity-biased due to the influence of freshwater inputs, which decreases the salinity at both sites. We advise using this proxy far from the river mouths to reduce the influence of the salinity on foraminiferal assemblages. Likely, the redox-sensitivity of elements such as vanadium is obscured by the dominant supply of detrital elements in proximal environments.

However, a proxy for hypoxia derived from the size distribution of sedimentary framboidal pyrites provides clear indications of the oxygenation state of the water column. Indeed, the absence of framboidal pyrites in the core located near the Danube mouth (GC7) suggests permanent oxic conditions at least over the last ~1750 years. This is in agreement with the low pyrite iron content ($6 \pm 2\%$ of reactive iron) measured by sequential extraction. On the contrary, a downward increase in pyrite iron content (from 20% up to 80% of reactive iron) was observed in the other core (GC15). In addition, the two size ranges of framboidal pyrites measured in this core evidence that bottom waters experienced alternating oxic/dysoxic (mean pyrite diameter $6-10 \pm 3-5 \mu\text{m}$) and anoxic (mean pyrite diameter $3-6 \pm 1-2 \mu\text{m}$) conditions during the last ~7400 years. These reducing conditions are supported by the slight enrichment in U of the sediment. Euxinic conditions were unlikely given that no Mo enrichment was measured.

Thus, the framboidal pyrite proxy revealed different oxygenation conditions over the Holocene for the two sites investigated. Moreover, our study confirms that the size of framboidal pyrites observed in the NW Black Sea coastal sediments can be used as a proxy to detect hypoxia or anoxia even in a proximal environment.

As stated by Rickard [39], new data are required for recent sediments collected from basins exhibiting various degrees of oxygenation in order to improve our understanding of the process of formation, growth and preservation of framboidal pyrite proxies and the statistical robustness of proxies derived from their characteristics. Further research should determine (1) if small frambooids can form in the water column during episodic anoxic events, (2) if big frambooids can form within the sediment under seasonally hypoxic conditions, (3) if a few days or weeks of anoxia or hypoxia per year are sufficient to produce frambooids and (4) if these frambooids are preserved in the sediment during oxic periods. To validate the use of framboidal pyrite as a proxy for past seasonal hypoxia, sediments from multicores should be studied at locations across the NW Black Sea shelf, and sediment traps should be deployed during hypoxic events in order to determine if some framboidal pyrites form in the water column.

Author Contributions: Conceptualisation: A.C., L.C., M.G. and N.F.; funding acquisition: M.G., N.F. and L.C.; investigation: S.R., A.O.M., N.P. and N.F.; methodology: A.C., L.C., M.G. and N.F.; project administration: M.G.; resources: S.R., A.O.M., L.C., F.F., G.L., N.P., A.P. and O.R.R.; supervision: N.F.; visualisation: S.R. and A.O.M.; writing—original draft: S.R. and A.O.M.; writing—review and editing: S.R., A.O.M., A.C., L.C., M.G., N.P. and N.F. All authors have read and agreed to the published version of the manuscript.

Funding: This research was funded by the FNRS (PDR T.1009.15, 2015–2019) in the framework of the BenthOx project. The cores used in this article were retrieved during a survey of the EMBLAS-II project (funded by the EU and UNDP).

Data Availability Statement: Not applicable.

Acknowledgments: This paper is an outcome of the FNRS BENTHOX project grant T.1009.15. The authors wish to thank Isabelle Billy (University of Bordeaux) for helping with the XRF core scanner and SCOPIX measurement, Laurence Monin (Musée Royal d’Afrique Centrale) for her explanations about the ICP-MS, ICP-OES and LA-ICP-MS, Frédéric Boulvain (University of Liège) for his assistance with the observation and interpretation of the thin sections, Joël Otten (University of Liège) for his help in sedimentological analyses, Barbara Sensula (Silesian University of Technology) for her explanations about the radiocarbon dating, Sabine Schmidt (University of Bordeaux) for her explanations about the ^{210}Pb method, Jemaa Amakrane (University Mohammed Premier) for giving advice about the identification of the foraminifera and Aurélia Hubert-Ferrari (University of Liège) for reviewing the manuscript. The three anonymous reviewers are gratefully acknowledged for their constructive suggestions and comments, which improved the clarity and readability of our manuscript.

Conflicts of Interest: The authors declare no conflict of interest. The funders had no role in the design of the study; in the collection, analyses, or interpretation of data; in the writing of the manuscript, or in the decision to publish the results.

Appendix A

Table A1. Results of the ^{210}Pb dating on MC7 and GC15 by the EPOC laboratory (University of Bordeaux, France). The dating at 25 cm depth in GC15 was derived from the other ^{210}Pb dates carried out on GC15 samples. The dating was performed on the fine (<63 μm) organic fraction of the sediment (OF).

Core	Depth (cm)	Material Dated	^{210}Pb cal BP	Error	Inferred Sedimentation Rate (cm/year)	Included in the Model Age
MC7	0.5	OF	2015	5	0.41	Yes
	4	OF	2006	5		Yes
	8	OF	1997	5		Yes
GC15	0.5	OF	2015	5	0.65	No
	10.5	OF	2000	5		No
	20.5	OF	1984	5		No
	28	OF	1973	5		No
	32	OF	1967	5		No
	34	OF	1963	5		No
	25	/		1977		5

Table A2. Results of ¹⁴C dating performed on GC7 and GC15 by the GADAM Centre (Silesian University of Technology, Poland). The dating conducted on the fine (<63 μm) organic fraction of the sediment (OF) and on bivalve shells. The WiTi¹⁴C age corresponds to the weighted average of the ¹⁴C age of two samples from the same depth. The Local ΔR is the local reservoir effect correction estimated either from the Marine Reservoir Correction Database (<http://calib.org/marine/>, accessed on October 24, 2019), based on Siani et al. [32] and Jones et al. [33] or from δ¹³C measurements conducted on bivalve shells from GC15. The *Deviation_{OF-shell}* is the shift between the ¹⁴C shell age and the ¹⁴C OF age.

Core	Laboratory ID	Depth (cm)	Material Dated	¹⁴ C Age (BP)	Error	WiTi ¹⁴ C Age (BP)	Ranges of Calendar Age for 95.4% Confidence Level	Local ΔR	<i>Deviation_{OF-shell}</i>
GC7	GdA-5385	41	OF	2930	45	2730 ± 35	2704 BP (95.4%) 2361 BP	126 ± 40 ^a	/
	GdA-5812		OF	2640	30		2842 BP (2.5%) 2825 BP–2794 BP (92.9%) 2735 BP		
	GdA-5813	98.5	OF	3960	45	/	4526 BP (93.5%) 4284 BP–4272 BP (1.9%) 4256 BP	/	/
	GdA-5037	117.5	Shell	665	30	/	675 BP (50.1%) 630 BP–600 BP (45.3%) 560 BP	126 ± 40 ^a	2950 ± 60
	GdA-5814		OF	3615	50	/	4088 BP (94.1%) 3826 BP–3788 BP (0.9%) 3776 BP–3740 BP (0.4%) 3734 BP		
	GdA-5386	150.5	OF	4490	35	/	4697 BP (95.4%) 4360 BP	/	2950 ± 60
	GdA-5815	171.5	OF	4760	50	/	5594 BP (75.1%) 5446 BP	/	2950 ± 60
	GdA-5387	210.5	OF	4200	45	/	4300 BP (95.4%) 3920 BP	/	/
GC15	GdA-5040	57	Shells	2110	30	2260 ± 30	1698 BP (7.3%) 1645 BP–1638 BP (88.1%) 1380 BP	13 ± 60 ^b	–690 ± 50
	GdA-5816A		Shells	2410	30		2139 BP (95.4%) 1816 BP		
	GdA-5816		OF	1570	40	/	1548 BP (95.4%) 1378 BP		
	GdA-5388	131.5	OF	6525	35	/	7020 BP (95.4%) 6724 BP	57 ± 85 ^a	/
	GdA-5817A	166.5	Shells	6365	35	/	6792 BP (95.4%) 6466 BP	135 ± 60 ^b	765 ± 57
	GdA-5817		OF	7130	45	/	8024 BP (79.7%) 7916 BP–7905 BP (15.7%) 7854 BP		
	GdA-5389	191.5	OF	8385	40	/	8970 BP (95.4%) 8614 BP	57 ± 85 ^a	/
	GdA-5818A	220.5	Shells	6505	40	/	7144 BP (0.9%) 7129 BP–7011 BP (94.5%) 6664 BP	106 ± 60 ^b	1270 ± 72
	GdA-5818		OF	7775	60	/	8700 BP (2.2%) 8669 BP–8658 BP (93.2%) 8415 BP		
	GdA-5819A	259.5	Shells	6745	45	/	7276 BP (95.4%) 6912 BP	130 ± 60 ^b	1015 ± 64
GdA-5819	OF		7760	55	/	8632 BP (95.4%) 8422 BP			
GdA-5390	280.5	OF	7780	40	/	8258 BP (95.4%) 7979 BP	57 ± 85 ^a	/	

^a Estimated from the Marine Reservoir Correction Database (<http://calib.org/marine/>, accessed on October 24, 2019), based on Siani et al. [32] and Jones and Gagnon [33]. ^b Estimated from δ¹³C measurements on bivalve shells from GC15, based on the method of Soulet et al. [34].

Table A3. Carbon and nitrogen contents and C/N atomic ratio in the GC15 and GC7 cores.

GC15				GC7			
Depth [cm]	% N	% C	C/N Atomic Ratio	Depth [cm]	% N	%C	C/N Atomic Ratio
1–5	0.19	2.0	12.3	0–1	0.14	1.5	13.1
5–10	0.20	2.2	13.1	1–2	0.12	1.2	11.7
10–12	0.20	2.2	12.8	2–3	0.13	1.0	9.7
12–14	0.19	2.0	12.2	3–4	0.12	0.9	9.4
14–16	0.21	2.0	11.3	4–5	0.14	1.2	10.0
16–18	0.20	2.1	11.9	5–6.5	0.14	1.3	10.9
18–20	0.22	2.2	11.7	6.5–8	0.12	1.1	11.0
20–22	0.19	2.1	12.6	8–9	0.12	1.0	10.2
22–24	0.20	2.1	12.2	9–10	0.12	1.1	10.4
24–26	0.19	2.2	13.5	10–11	0.13	1.1	9.5
26–28	0.20	2.3	13.7	11–12	0.15	1.2	9.7
28–30	0.21	2.3	12.9	12–13	0.15	1.3	10.3
30–32	0.17	2.2	15.3	13–14	0.14	1.4	11.7
32–34	0.19	2.1	13.2	14–15	0.15	1.3	10.1
34–36	0.21	2.3	12.9	15–16	0.16	1.5	10.7
36–38	0.20	2.2	13.1	16–17	0.14	1.3	10.6
38–40	0.20	1.8	10.3	17–18	0.16	1.6	11.2
40–42	0.23	2.2	11.0	18–19	0.13	1.2	11.1
42–44	0.20	2.0	11.7	19–20	0.14	1.3	10.4
44–46	0.19	1.8	11.0	20–21	0.15	1.7	12.9
46–48	0.18	2.4	15.4	21–22	0.09	0.9	11.7
48–50	0.14	2.5	20.9	22–23	0.14	1.3	11.0
50–52	0.16	2.5	17.6	23–24	0.12	1.0	9.8
52–54	0.18	2.2	14.5	24–25	0.13	1.1	9.8
54–56	0.13	1.9	16.6	25–26	0.12	0.9	9.0
56–58	0.20	2.1	12.3	26–28	0.11	0.8	8.6
104–105	0.13	1.2	9.0	28–29	0.15	1.3	10.5
107–108	0.12	0.9	7.3	29–30	0.14	1.2	10.7
132–133	0.14	1.0	7.3	30–31	0.14	1.2	9.9
151–152	0.06 *	0.5	7.4 *	31–32	0.14	1.2	9.7
167–168	0.07 *	0.5	7.0 *	32–33	0.15	1.1	9.0
175–176	0.07 *	0.5	7.7 *	33–34.5	0.13	1.0	9.2
				34.5–35.5	0.15	1.4	10.9
				35.5–36.5	0.11	1.0	10.3
				36.5–37.5	0.12	1.0	9.3
				37.5–38.5	0.11	0.9	9.8
				38.5–39.5	0.13	1.1	9.3
				39.5–40.5	0.13	1.0	8.9
				40.5–41.5	0.13	1.1	9.7
				41.5–42.5	0.08	0.6	8.8
				42.5–43.5	0.09	0.8	10.8
				43.5–44.5	0.11	0.9	8.8
				44.5–45.5	0.11	0.8	8.3
				45.5–46.5	0.12	1.0	9.5
				46.5–47.5	0.11	0.8	9.2
				47.5–48.5	0.11	0.8	8.2
				48.5–49.5	0.11	0.8	8.0
				49.5–50.5	0.11	0.8	8.7

Table A3. Cont.

GC15				GC7			
Depth [cm]	% N	% C	C/N Atomic Ratio	Depth [cm]	% N	%C	C/N Atomic Ratio
				50.5–51.5	0.13	1.2	10.2
				51.5–52.5	0.13	1.2	10.0
				52.5–53.5	0.13	1.0	9.5
				53.5–54.5	0.10	1.0	11.2
				54.5–55.5	0.10	0.8	9.2
				55.5–56.5	0.10	0.9	9.6
				56.5–57.5	0.12	1.0	10.1
				57.5–58.5	0.13	1.0	8.8
				58.5–59.5	0.15	1.2	9.6
				59.5–60.5	0.16	1.3	9.3
				60.5–61.5	0.14	1.1	9.3
				61.5–62.5	0.12	1.0	9.7
				62.5–63.5	0.13	0.9	8.5
				63.5–64.5	0.12	1.2	11.6
				64.5–65.5	0.16	1.5	10.7
				65.5–66.5	0.17	1.3	9.3
				66.5–67.5	0.12	0.9	8.9
				67.5–68.5	0.13	1.0	9.3
				68.5–69.5	0.14	1.1	9.7
				69.5–70.5	0.14	1.1	9.1
				70.5–71.5	0.16	1.6	11.9
				71.5–72.5	0.14	1.3	10.6
				72.5–73.5	0.13	1.0	9.0
				73.5–74.5	0.16	1.4	10.1
				74.5–75.5	0.14	1.2	10.2
				75.5–76.5	0.08	0.7	9.3
				76.5–77.5	0.11	1.1	10.9
				77.5–78.5	0.12	1.3	12.1
				78.5–79.5	0.13	1.2	11.0
				79.5–81	0.14	1.2	10.5
				81–82	0.12	1.0	9.8
				82–83	0.13	1.3	11.9
				83–84	0.13	1.1	9.4
				84–85	0.13	1.2	10.6
				85–86	0.13	1.4	12.7
				86–87.5	0.15	1.3	10.4
				87.5–88.5	0.13	1.3	11.5
				88.5–89.5	0.13	1.1	9.9
				89.5–90.5	0.13	1.2	10.3
				90.5–91.5	0.13	1.1	9.4
				91.5–92.5	0.13	0.9	8.7
				92.5–93.5	0.15	1.6	12.3
				93.5–94.5	0.16	1.5	11.1
				94.5–97	0.14	1.3	11.1
				107–108	0.07 *	0.5	7.9 *
				126–127	0.09 *	0.7	7.7 *
				145–146	0.08 *	0.8	10.3 *
				179–180	0.10 *	0.8	8.2 *

* low N content leading to a less reliable C/N value.

Table A4. Number of *Ammonia*, *Elphidium* and *Nonion* foraminifera counted in GC7 and GC15 samples with the calculated values of the A-E index (for the fraction > 150 μm). Total foraminifera includes non-identified individuals (minor genus or badly preserved).

Core	Depth (cm)	Number of Foraminifera				A-E Index (N _A /(N _A + N _E)) × 100
		<i>Ammonia</i> N _A	<i>Elphidium</i> N _E	<i>Nonion</i>	Total	
GC7	28–29	12	1	0	17	92
	43.5–44.5	6	0	0	9	100
	101–102	59	1	0	66	98
	112–113	25	0	1	29	100
	126–127	13	0	0	13	100
	133–134	32	0	1	36	100
	134–135	31	0	0	37	100
	151–152	49	0	0	49	100
	163–164	198	1	0	200	99
	165–166	6	0	0	6	100
	179–180	57	0	1	58	100
204–205	6	0	0	6	100	
GC15	42–44	184	3	11	199	98
	50–52	170	11	19	200	94
	134–135	193	4	3	200	98
	147–148	147	0	1	151	100
	163–164	58	1	1	60	98
	165–166	182	3	14	200	98
	167–168	189	0	5	194	100
187–188	190	3	7	200	98	

Table A5. Reactive iron speciation (Fe_{reactive}) for the GC15 and GC7 cores. Fe_H (easily extractable fraction with labile ferrous, i.e., FeS and siderite, and ferric iron, i.e., ferrihydrite, akaganeite and lepidocrocite), Fe_{org} (iron bound to organic matter), Fe_{ox} (hematite and goethite) and Fe_{pyr} (pyrite).

GC15						GC7					
Depth	Fe _{reactive}	Fe _H	Fe _{org}	Fe _{ox}	Fe _{pyr}	Depth	Fe _{reactive}	Fe _H	Fe _{org}	Fe _{ox}	Fe _{pyr}
[cm]	[% of Fe _{total}]	[% of Fe _{reactive}]				[cm]	[% of Fe _{total}]	[% of Fe _{reactive}]			
14–16	32	46	9	25	20	28–29	41	86	7	1	7
18–20	34	47	9	21	23	43.5–44.5	*	79	10	1	9
24–26	38	44	8	18	30	101–102	*	85	6	1	7
28–30	33	50	6	5	39	107–108	34	83	9	2	6
34–36	37	45	7	5	44	113–114	33	87	6	1	6
40–42	36	55	8	4	33	126–127	*	89	5	1	5
50–52	*	39	6	2	53	133–134	*	91	4	1	4
56–58	55	36	5	3	56	145–146	*	91	4	1	4
104–105	41	10	8	4	79	151–152	*	90	4	1	4
107–108	38	7	10	4	79	179–180	*	86	6	2	7
132–133	36	10	8	4	78	204–205	*	91	5	1	3
151–152	32	8	9	4	80	Mean ± SD	36 ± 4	87 ± 4	6 ± 2	1 ± 0.4	6 ± 2
163–164	*	26	8	2	65						
167–168	37	8	8	3	81						
175–176	39	6	10	3	81						
Mean ± SD	38 ± 6	26 ± 19	8 ± 1	5 ± 8	61 ± 23						

* Total iron not measured.

Table A6. Size distribution of the diameters of framboidal pyrites in 15 samples from GC15 (30 diameters) and one sample from MC15 (8 diameters).

Depth [cm]	Number of Framboidal Pyrites per Classes of Diameters Measured in μm																				Mean Diameter \pm SD [μm]		
	[1, 2]	[2, 3]	[3, 4]	[4, 5]	[5, 6]	[6, 7]	[7, 8]	[8, 9]	[9, 10]	[10, 11]	[11, 12]	[12, 13]	[13, 14]	[14, 15]	[15, 16]	[16, 17]	[17, 18]	[18, 19]	[19, 20]	[20, 21]		[21, 22]	
1–5	1	2	3	6	8	4	4	/	2	/	/	/	/	/	/	/	/	/	/	/	/	5.4 \pm 1.9	
10–12	/	3	7	/	6	8	1	2	2	/	1	/	/	/	/	/	/	/	/	/	/	5.8 \pm 2.3	
18–20	1	1	5	4	7	5	1	4	/	2	/	/	/	/	/	/	/	/	/	/	/	5.7 \pm 2.2	
28–30	/	1	1	6	5	7	2	2	1	/	/	/	/	1	/	/	/	/	/	2	1	1	8.1 \pm 5.4
40–42	/	/	3	4	13	3	3	3	1	/	/	/	/	/	/	/	/	/	/	/	/	6.0 \pm 1.6	
50–52	/	/	3	9	7	5	3	2	/	1	/	/	/	/	/	/	/	/	/	/	/	5.6 \pm 1.6	
104–105	1	7	14	7	1	/	/	/	/	/	/	/	/	/	/	/	/	/	/	/	/	3.5 \pm 0.8	
132–133	2	8	12	4	3	/	1	/	/	/	/	/	/	/	/	/	/	/	/	/	/	3.6 \pm 1.2	
141–142	/	1	6	4	6	3	3	1	/	/	1	/	/	2	/	/	/	/	/	/	/	6.4 \pm 3.0	
151–152	/	1	5	2	7	5	2	2	1	1	1	/	/	1	/	/	/	1	/	/	1	7.2 \pm 4.3	
163–164	/	3	8	11	5	2	1	/	/	/	/	/	/	/	/	/	/	/	/	/	/	4.5 \pm 1.2	
175–176	/	3	2	4	16	3	2	/	/	/	/	/	/	/	/	/	/	/	/	/	/	5.2 \pm 1.2	
186–187	/	/	4	5	12	4	2	/	/	/	/	/	/	/	1	2	/	/	/	/	/	6.4 \pm 3.5	
196–197	/	2	3	5	6	6	4	3	/	1	/	/	/	/	/	/	/	/	/	/	/	5.8 \pm 1.9	
268–269	/	1	1	7	12	6	/	2	/	1	/	/	/	/	/	/	/	/	/	/	/	5.7 \pm 1.5	
MC15: 2–4	/	/	1	1	1	/	/	2	1	1	/	/	/	/	/	/	/	/	/	/	/	not enough data	

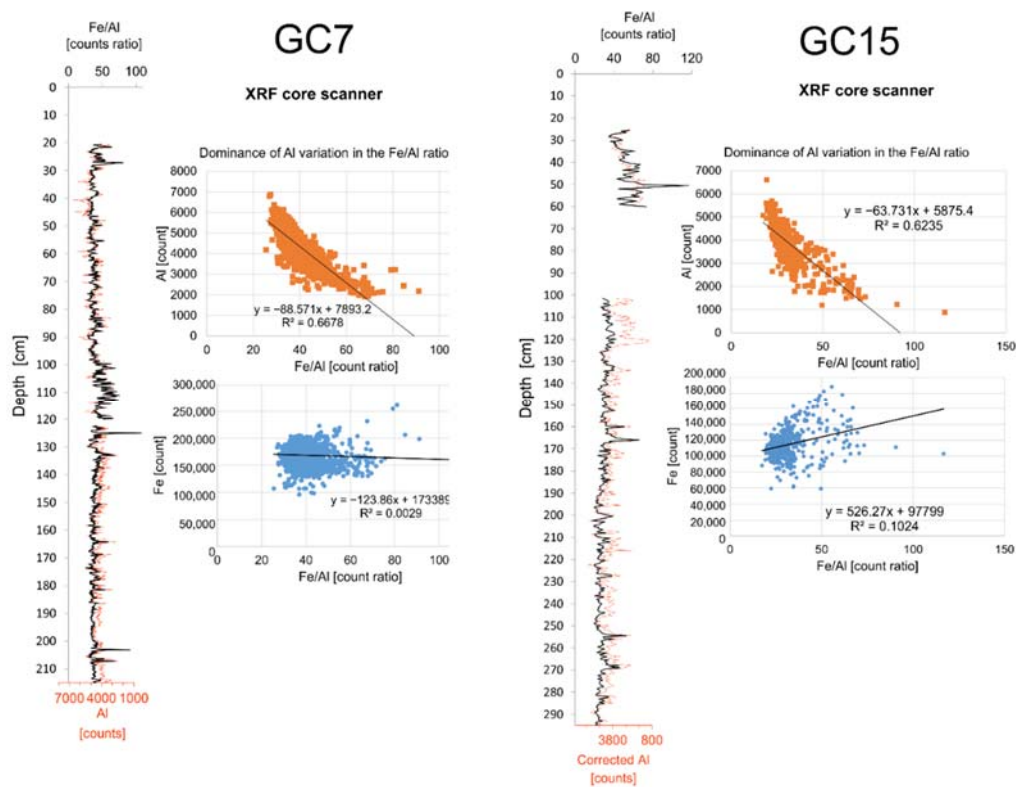


Figure A1. Domination of Al variations in the Fe/Al ratio in XRF core scanner measurements illustrated by the high correlation between Al count and Fe/Al count ratio in GC7 ($R^2 = 0.67$) and in GC15 ($R^2 = 0.62$), while in contrast, there is no correlation between Fe and Fe/Al ($R^2 = 0$ and 0.10 respectively for GC7 and GC15).

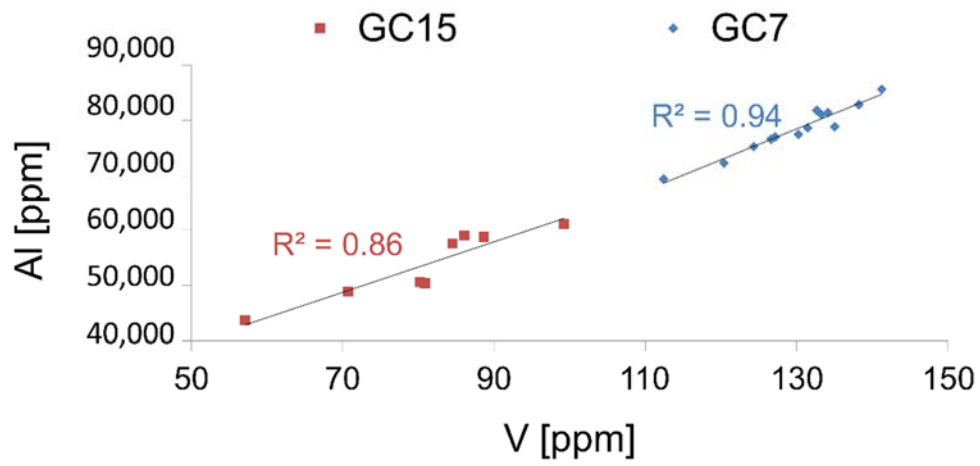


Figure A2. Correlation between aluminium (Al, measured by ICP-OES) and vanadium (V, measured by ICP-MS) contents for the GC7 core (14 samples) and the GC15 core (8 samples).

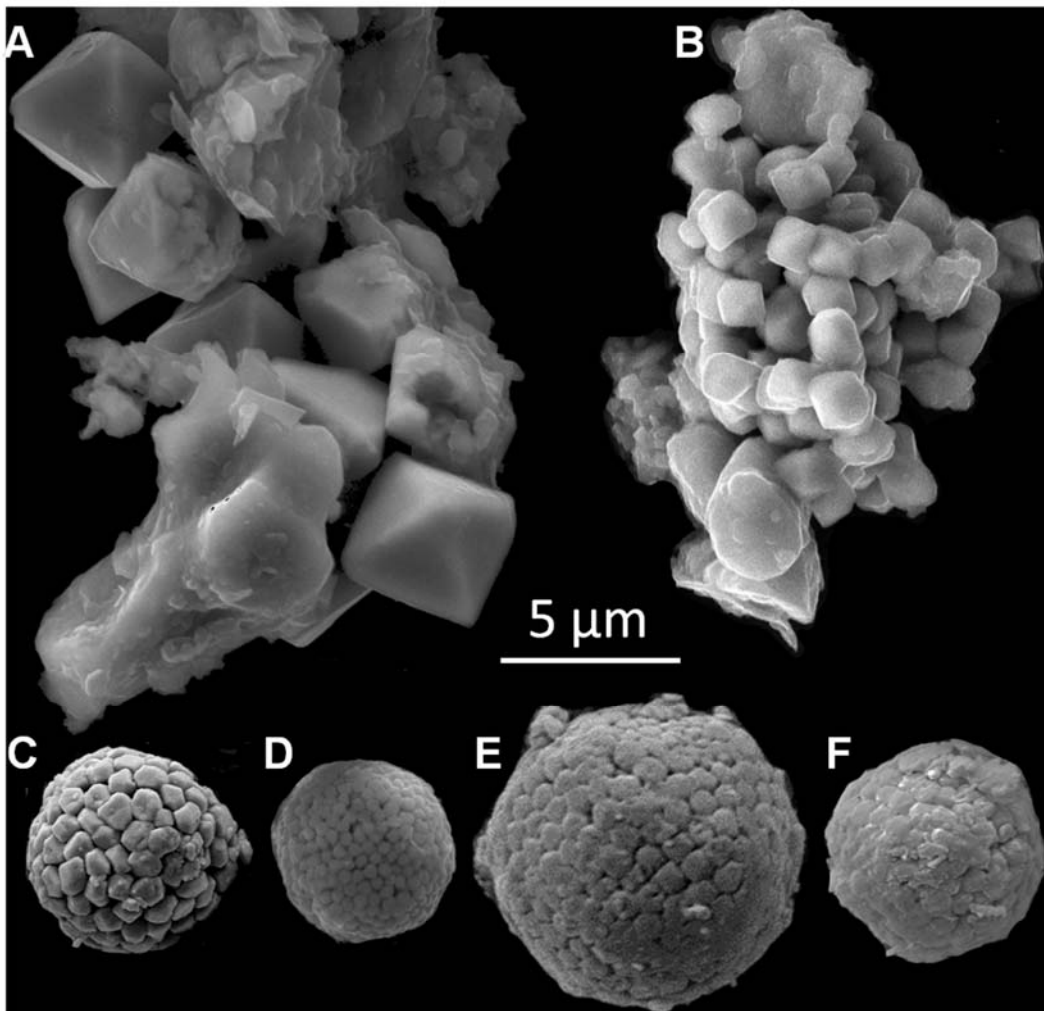


Figure A3. Cont.

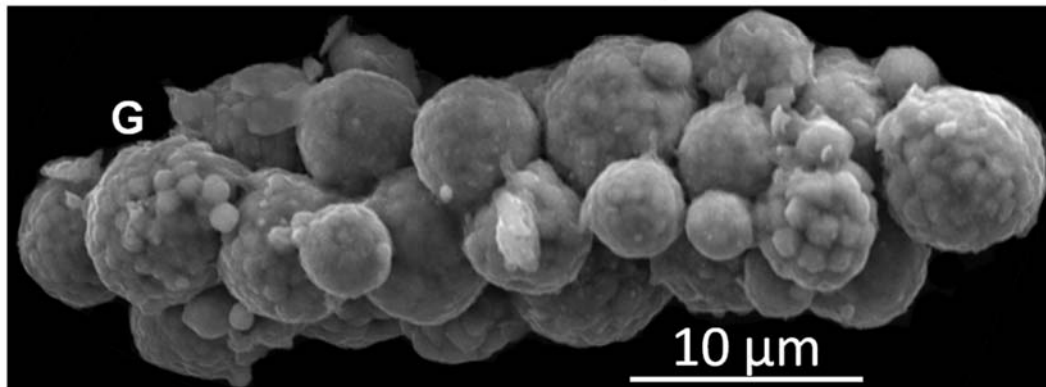


Figure A3. SEM images of different pyrite morphologies observed in the GC15 core: (A) octahedral 4 μm wide pyrite crystals (sample: 151–152 cm depth, secondary electron mode, C coating); (B) loose aggregate of 1.5 μm wide pyrite microcrystals (sample: 132–133 cm depth, back-scattered electron mode, C coating); (C) 6 μm wide framboidal pyrite composed of 0.6 to 1 μm -wide microcrystals (sample: 36–38 cm depth, secondary electron mode, Au metallisation); (D) 5 μm wide framboidal pyrite composed of 0.4 μm wide microcrystals (sample: 1–5 cm depth, secondary electron mode, C coating); (E) 9 μm wide partially filled-in framboidal pyrite composed of 0.8 μm wide microcrystals (sample: 36–38 cm, secondary electron mode, Au metallisation); (F) 6 μm wide filled-in framboidal pyrite (sample: 54–56 cm depth, secondary electron mode, Au metallisation); (G) cluster including more than 25 framboidal pyrites from 2 to 7 μm wide composed of multiple size microcrystals (e.g., 0.7 or 1.2 μm), some framboids are filled-in (sample: 186–187 cm, secondary electron mode, C coating).

References

- Breitbart, D.; Levin, L.A.; Oschlies, A.; Grégoire, M.; Chavez, F.P.; Conley, D.J.; Garçon, V.; Gilbert, D.; Gutiérrez, D.; Isensee, K.; et al. Declining Oxygen in the Global Ocean and Coastal Waters. *Science* **2018**, *359*, eaam7240. [[CrossRef](#)] [[PubMed](#)]
- Diaz, R.; Rosenberg, R. Marine Benthic Hypoxia: A Review of Its Ecological Effects and the Behavioural Response of Benthic Macrofauna. *Oceanogr. Mar. Biol. Annu. Rev.* **1995**, *33*, 245–303.
- Kemp, W.M.; Testa, J.M.; Conley, D.J.; Gilbert, D.; Hagy, J.D. Temporal Responses of Coastal Hypoxia to Nutrient Loading and Physical Controls. *Biogeosciences* **2009**, *6*, 2985–3008. [[CrossRef](#)]
- Wilkin, R.T.; Barnes, H.L. Formation Processes of Framboidal Pyrite. *Geochim. Cosmochim. Acta* **1997**, *61*, 323–339. [[CrossRef](#)]
- Arthur, M.A.; Dean, W.E. Organic-Matter Production and Preservation and Evolution of Anoxia in the Holocene Black Sea. *Paleoceanography* **1998**, *13*, 395–411. [[CrossRef](#)]
- Wegwerth, A.; Eckert, S.; Dellwig, O.; Schnetger, B.; Severmann, S.; Weyer, S.; Brüske, A.; Kaiser, J.; Köster, J.; Arz, H.W.; et al. Redox Evolution during Eemian and Holocene Sapropel Formation in the Black Sea. *Palaeogeogr. Palaeoclimatol. Palaeoecol.* **2018**, *489*, 249–260. [[CrossRef](#)]
- Konovalov, S.K.; Murray, J.W. Variations in the Chemistry of the Black Sea on a Time Scale of Decades (1960–1995). *J. Mar. Syst.* **2001**, *31*, 217–243. [[CrossRef](#)]
- Lyons, T.W.; Berner, R.A.; Anderson, R.F. Evidence for Large Pre-Industrial Perturbations of the Black Sea Chemocline. *Nature* **1993**, *365*, 538–540. [[CrossRef](#)]
- Huang, Y.; Freeman, K.H.; Wilkin, R.T.; Arthur, M.A.; Jones, A.D. Black Sea Chemocline Oscillations during the Holocene: Molecular and Isotopic Studies of Marginal Sediments. *Org. Geochem.* **2000**, *31*, 1525–1531. [[CrossRef](#)]
- Ukrainskii, V.V.; Popov, Y.I. Climatic and Hydrophysical Conditions of the Development of Hypoxia in Waters of the Northwest Shelf of the Black Sea. *Phys. Oceanogr.* **2009**, *19*, 140. [[CrossRef](#)]
- Panin, N.; Jipa, D. Danube River Sediment Input and Its Interaction with the North-Western Black Sea. *Estuar. Coast. Shelf Sci.* **2002**, *54*, 551–562. [[CrossRef](#)]
- Friedrich, J.; Dinkel, C.; Friedl, G.; Pimenov, N.; Wijsman, J.; Gomoiu, M.-T.; Cociasu, A.; Popa, L.; Wehrli, B. Benthic Nutrient Cycling and Diagenetic Pathways in the North-Western Black Sea. *Estuar. Coast. Shelf Sci.* **2002**, *54*, 369–383. [[CrossRef](#)]
- Capet, A.; Beckers, J.-M.; Grégoire, M. Drivers, Mechanisms and Long-Term Variability of Seasonal Hypoxia on the Black Sea Northwestern Shelf – Is There Any Recovery after Eutrophication? *Biogeosciences* **2013**, *10*, 3943–3962. [[CrossRef](#)]
- Gooday, A.J.; Jorissen, F.; Levin, L.A.; Middelburg, J.J.; Naqvi, S.W.A.; Rabalais, N.N.; Scranton, M.; Zhang, J. Historical Records of Coastal Eutrophication-Induced Hypoxia. *Biogeosciences* **2009**, *6*, 1707–1745. [[CrossRef](#)]
- Zillén, L.; Conley, D.J.; Andrén, T.; Andrén, E.; Björck, S. Past Occurrences of Hypoxia in the Baltic Sea and the Role of Climate Variability, Environmental Change and Human Impact. *Earth-Sci. Rev.* **2008**, *91*, 77–92. [[CrossRef](#)]

16. Sen Gupta, B.K.; Eugene Turner, R.; Rabalais, N.N. Seasonal Oxygen Depletion in Continental-Shelf Waters of Louisiana: Historical Record of Benthic Foraminifers. *Geology* **1996**, *24*, 227–230. [[CrossRef](#)]
17. Middelburg, J.J.; Levin, L.A. Coastal Hypoxia and Sediment Biogeochemistry. *Biogeosciences* **2009**, *6*, 1273–1293. [[CrossRef](#)]
18. Tribovillard, N.; Algeo, T.J.; Lyons, T.; Riboulleau, A. Trace Metals as Paleoredox and Paleoproductivity Proxies: An Update. *Chem. Geol.* **2006**, *232*, 12–32. [[CrossRef](#)]
19. Wilkin, R.T.; Barnes, H.L.; Brantley, S.L. The Size Distribution of Framboidal Pyrite in Modern Sediments: An Indicator of Redox Conditions. *Geochim. Cosmochim. Acta* **1996**, *60*, 3897–3912. [[CrossRef](#)]
20. Bond, D.P.G.; Wignall, P.B. Pyrite Framboid Study of Marine Permian–Triassic Boundary Sections: A Complex Anoxic Event and Its Relationship to Contemporaneous Mass Extinction. *GSA Bull.* **2010**, *122*, 1265–1279. [[CrossRef](#)]
21. Rabalais, N.N.; Turner, R.E.; Justić, D.; Dortch, Q.; Wiseman, W.J.; Sen Gupta, B.K. Nutrient Changes in the Mississippi River and System Responses on the Adjacent Continental Shelf. *Estuaries* **1996**, *19*, 386–407. [[CrossRef](#)]
22. Yanko-Hombach, V.V. Controversy over Noah’s Flood in the Black Sea: Geological and Foraminiferal Evidence from the Shelf. In *The Black Sea Flood Question: Changes in Coastline, Climate, and Human Settlement*; Yanko-Hombach, V., Gilbert, A.S., Panin, N., Dolukhanov, P.M., Eds.; Springer: Dordrecht, The Netherlands, 2007; pp. 149–203. ISBN 978-1-4020-5302-3.
23. Jilbert, T.; Slomp, C.P. Rapid High-Amplitude Variability in Baltic Sea Hypoxia during the Holocene. *Geology* **2013**, *41*, 1183–1186. [[CrossRef](#)]
24. Dijkstra, N.; Slomp, C.P.; Behrends, T. Vivianite Is a Key Sink for Phosphorus in Sediments of the Landsort Deep, an Intermittently Anoxic Deep Basin in the Baltic Sea. *Chem. Geol.* **2016**, *438*, 58–72. [[CrossRef](#)]
25. Van Helmond, N.A.G.M.; Jilbert, T.; Slomp, C.P. Hypoxia in the Holocene Baltic Sea: Comparing Modern versus Past Intervals Using Sedimentary Trace Metals. *Chem. Geol.* **2018**, *493*, 478–490. [[CrossRef](#)]
26. Spofforth, D.J.A.; Pälke, H.; Green, D. Paleogene Record of Elemental Concentrations in Sediments from the Arctic Ocean Obtained by XRF Analyses. *Paleoceanography* **2008**, *23*, PA1S09. [[CrossRef](#)]
27. Kraal, P.; Burton, E.D.; Bush, R.T. Iron Monosulfide Accumulation and Pyrite Formation in Eutrophic Estuarine Sediments. *Geochim. Cosmochim. Acta* **2013**, *122*, 75–88. [[CrossRef](#)]
28. Kalliokoski, J.; Cathles, L. Morphology, Mode of Formation, and Diagenetic Changes in Framboids. *Bull. Geol. Soc. Finl.* **1969**, *41*, 125–133. [[CrossRef](#)]
29. Plante, A. *Marine Benthic Hypoxia and Its Consequences for Sediment-Water Exchanges and Early Diagenesis*; Université de Liège: Liège, Belgium, 2020.
30. Krishnaswamy, S.; Lal, D.; Martín, J.; Meybeck, M. Geochronology of Lake Sediments. *Earth Planet. Sci. Lett.* **1971**, *11*, 407–414. [[CrossRef](#)]
31. Reimer, P.J.; Bard, E.; Bayliss, A.; Beck, J.W.; Blackwell, P.G.; Ramsey, C.B.; Buck, C.E.; Cheng, H.; Edwards, R.L.; Friedrich, M.; et al. IntCal13 and Marine13 Radiocarbon Age Calibration Curves 0–50,000 Years Cal BP. *Radiocarbon* **2013**, *55*, 1869–1887. [[CrossRef](#)]
32. Siani, G.; Paterne, M.; Arnold, M.; Bard, E.; Métivier, B.; Tisnerat, N.; Bassinot, F. Radiocarbon Reservoir Ages in the Mediterranean Sea and Black Sea. *Radiocarbon* **2000**, *42*, 271–280. [[CrossRef](#)]
33. Jones, G.A.; Gagnon, A.R. Radiocarbon Chronology of Black Sea Sediments. *Deep Sea Res. Part Oceanogr. Res. Pap.* **1994**, *41*, 531–557. [[CrossRef](#)]
34. Soulet, G.; Giosan, L.; Flaux, C.; Galy, V. Using Stable Carbon Isotopes to Quantify Radiocarbon Reservoir Age Offsets in the Coastal Black Sea. *Radiocarbon* **2019**, *61*, 309–318. [[CrossRef](#)]
35. Blaauw, M. Methods and Code for ‘Classical’ Age-Modelling of Radiocarbon Sequences. *Quat. Geochronol.* **2010**, *5*, 512–518. [[CrossRef](#)]
36. McLennan, S.M. Relationships between the Trace Element Composition of Sedimentary Rocks and Upper Continental Crust. *Geochem. Geophys. Geosys.* **2001**, *2*, 1021. [[CrossRef](#)]
37. Claff, S.R.; Sullivan, L.A.; Burton, E.D.; Bush, R.T. A Sequential Extraction Procedure for Acid Sulfate Soils: Partitioning of Iron. *Geoderma* **2010**, *155*, 224–230. [[CrossRef](#)]
38. Lloyd, G.E. Atomic Number and Crystallographic Contrast Images with the SEM: A Review of Backscattered Electron Techniques. *Mineral. Mag.* **1987**, *51*, 3–19. [[CrossRef](#)]
39. Rickard, D. Sedimentary Pyrite Framboid Size-Frequency Distributions: A Meta-Analysis. *Palaeogeogr. Palaeoclimatol. Palaeoecol.* **2019**, *522*, 62–75. [[CrossRef](#)]
40. Leng, M.J.; Lewis, J.P. C/N Ratios and Carbon Isotope Composition of Organic Matter in Estuarine Environments. In *Applications of Paleoenvironmental Techniques in Estuarine Studies*; Weckström, K., Saunders, K.M., Gell, P.A., Skilbeck, C.G., Eds.; Developments in Paleoenvironmental Research; Springer: Dordrecht, The Netherlands, 2017; pp. 213–237. ISBN 978-94-024-0990-1.
41. Burton, E.D.; Bush, R.T.; Sullivan, L.A. Fractionation and Extractability of Sulfur, Iron and Trace Elements in Sulfidic Sediments. *Chemosphere* **2006**, *64*, 1421–1428. [[CrossRef](#)]
42. Sen Gupta, B.K.; Platon, E. Tracking Past Sedimentary Records of Oxygen Depletion in Coastal Waters: Use of the Ammonia-Elphidium Foraminiferal Index. *J. Coast. Res.* **2006**, *3*, 1351–1355.
43. Cronin, T.; Willard, D.; Karlsen, A.W.; Ishman, S.; Verardo, S.; McGeehin, J.; Kerhin, R.; Holmes, C.; Colman, S.; Zimmerman, A. Climatic Variability in the Eastern United States over the Past Millennium from Chesapeake Bay Sediments. *Geology* **2000**, *28*, 3–6. [[CrossRef](#)]

44. Armstrong, H.A.; Brasier, M.D. Foraminifera. In *Microfossils*; John Wiley & Sons, Ltd: Hoboken, NJ, USA, 2013; pp. 142–187. ISBN 978-1-118-68544-0.
45. Rothwell, R.G.; Croudace, I.W. Twenty Years of XRF Core Scanning Marine Sediments: What Do Geochemical Proxies Tell Us? In *Micro-XRF Studies of Sediment Cores: Applications of a Non-Destructive Tool for the Environmental Sciences*; Croudace, I.W., Rothwell, R.G., Eds.; Developments in Paleoenvironmental Research; Springer: Dordrecht, The Netherlands, 2015; pp. 25–102. ISBN 978-94-017-9849-5.
46. Poulton, S.W.; Canfield, D.E. Development of a Sequential Extraction Procedure for Iron: Implications for Iron Partitioning in Continentally Derived Particulates. *Chem. Geol.* **2005**, *214*, 209–221. [[CrossRef](#)]
47. Poulton, S.W.; Canfield, D.E. Ferruginous Conditions: A Dominant Feature of the Ocean through Earth's History. *Elements* **2011**, *7*, 107–112. [[CrossRef](#)]
48. Anderson, T.F.; Raiswell, R. Sources and Mechanisms for the Enrichment of Highly Reactive Iron in Euxinic Black Sea Sediments. *Am. J. Sci.* **2004**, *304*, 203–233. [[CrossRef](#)]
49. Van Helmond, N.A.G.M.; Quintana Krupinski, N.B.; Lougheed, B.C.; Obrochta, S.P.; Andrén, T.; Slomp, C.P. Seasonal Hypoxia Was a Natural Feature of the Coastal Zone in the Little Belt, Denmark, during the Past 8ka. *Mar. Geol.* **2017**, *387*, 45–57. [[CrossRef](#)]